# LASER INTERFEROMETRIC STUDY OF RAYLEIGH-BENARD CONVECTION IN AN AXISYMMETRIC DIFFERENTIALLY HEATED FLUID LAYER

by

Atul Srivastava
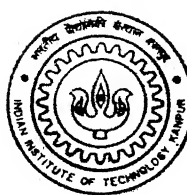
LASER TECHNOLOGY PROGRAMME
INDIAN INSTITUTE OF TECHNOLOGY KANPUR

April, 2000

LASER INTERFEROMETRIC STUDY OF RAYLEIGH-BENARD CONVECTION IN AN AXISYMMETRIC DIFFERENTIALLY HEATED FLUID LAYER

A THESIS SUBMITTED

IN PARTIAL FULFILMENT OF THE REQUIREMENTS

FOR THE DEGREE OF

MASTER OF TECHNOLOGY

by

Atul Srivastava

to the

LASER TECHNOLOGY PROGRAMME

INDIAN INSTITUTE OF TECHNOLOGY

KANPUR–208016 INDIA

APRIL 2000
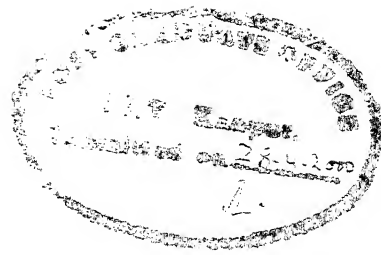
CERTIFICATE

It is certified that the work contained in the thesis entitled "*Laser Inter-ferometric Study of Rayleigh-Benard Convection in an Axisymmetric Differentially Heated Fluid Layer*", by *Mr. Atul Srivastava* , has been carried out under our supervision and that this work has not been submitted elsewhere for a degree.

K. Muralidhar
Professor
Dept. of Mechanical Engineering and
Laser Technology Programme
I.I.T. Kanpur 208016

P. K. Panigrahi
Asst. Professor
Dept. of Mechanical Engineering
I.I.T. Kanpur 208016

April, 2000

Abstract

Buoyancy-driven convection in a horizontal differentially heated fluid layer has been experimentally studied. The bounding faces of the fluid layer are maintained at different temperatures, thus producing an unstable configuration. The confining side walls are thermally insulated and have a constant radius. As a result, one is led to a circular, axisymmetric problem of Rayleigh-Benard convection.

Experiments have been conducted in a fluid layer of 64 cm diameter, 2.3 cm vertical height and temperature difference of $5 - 10^{o}C$. The working fluid is air. The dimensionless parameter governing the convection pattern, namely the Rayleigh number is in the range 6000 to 12000, corresponding to four to eight times the critical value. Experiments of this type play an important role in various applications including electronic packaging, solar ponds, waste heat disposal systems and atmospheric convection.

The convection patterns in the fluid layer have been visualised in the present work using the Mach-Zehnder interferometer. A 35 mW He-Ne laser has been used as the light source. The interferometer employs 150 mm diameter laser grade optics. The interferograms have been recorded using the CCD camera connected to an image processing system. Image acquisition is at video rates, namely 50 images per second. All interferograms have been recorded in the infinite fringe setting.

The present research is directed towards examining the following issues : (a) the influence of Rayleigh number on the steady (long time) thermal field, (b) the transient evolution of the thermal field at a given Rayleigh number, (c) comparision of the convection patterns in axisymmetric fluid layers and cavities square in plan, (d) asymmetry of the thermal field in an axisymmetric geometry and (e) comparision with a numerically generated solution of the flow and heat transfer problem. Results obtained show unexpected features in the thermal field, and important differences arising from the shape of the confining boundaries.

Acknowledgement

Contents

List of Figures

Nomenclature

g	Accelaration due to gravity
h	Height of the cavity
L	Distance traversed by the laser beam through the test cell
n	Refractive index of the fluid
n_o	Reference value of refractive index
Nu	Nusselt number (line-of-sight and surface averaged)
Pr	Prandtl number of the fluid, (ν/α)
Ra	Rayleigh number
s	Coordinates along an axis inclined at an angle to the x axis.
T	Temperature
T_o	Reference temperature
ΔT_ϵ	Temperature difference between successive fringes
r, z	Cylindrical co-ordinates
α	Thermal diffusivity of the fluid
β	Coefficient of volume expansion of the fluid
λ	Wavelength of the laser
ν	Kinematic viscocity of the fluid
ρ	Density of fluid
ρ_o	Reference value of density

Chapter 1

Introduction

Natural convection phenomena of Newtonian fluids confined in differentially heated enclosures have attracted considerable attention in recent times. Rayleigh-Benard convection is an appropriate model to understand the flow instabilities and laminar flow transitions that a fluid undergoes when subjected to some temperature gradient between its two surfaces.

In its simplest form, Rayleigh-Benard convection can be defined as the motion of the layer of fluid confined between two infinite horizontal walls heated from below and cooled from above, the sidewalls of the enclosure being adiabatic. This configuration results in an unstable stratification of the fluid layer with cold heavy fluid on top of the light hot fluid. The fluid layer thus has a natural tendency to readjust towards a stable cofiguration. The driving force responsible for the convective motion is buoyancy. When the buoyancy force is below a certain threshold the viscous forces between the fluid layers act as internal friction and inhibit fluid motion. Heat transfer across the fluid layer is then purely by conduction. Once the threshold value of buoyancy is exceeded, convective motion starts. The resulting flow pattern depends on the strength of buoyancy, fluid properties and the geometry of the confining boundaries.

The non-dimensional parameter <u>Rayleigh number</u> is the relative measure of the strength of the buoyancy force to viscous force. More fundamentally, it is the ratio of the work done by buoyancy in the gravity field to the viscous dissipation.

The Prandtl number is a second dimensionless quantity arising in thermal convection. It is a measure of ratio of the molecular diffusivity of momentum to that of thermal energy and is a fluid property. Flow transitions are generally documented in terms of Rayleigh number and Prandtl number. The Rayleigh number is defined as:

$$\mathrm{Ra} = \frac{g\beta(T_{hot} - T_{cold})h^3}{\nu\alpha} \tag{1.1}$$

and the Prandtl number:

$$\mathrm{Pr} = \frac{\nu}{\alpha} \tag{1.2}$$

The Rayleigh-Benard convection is an important mechanism of fluid flow and heat transfer in natural as well as many engineering systems. Its study is relevant to the disciplines of astrophysics, geophysics, atmospheric sciences and many practical systems related to various engineering applications. The phenomena of atmospheric convection like winds, cyclones, storms and monsoon can be modelled as Rayleigh-Benard convection with different latitudes of earth considered as isothermal walls and the movement of air caused by buoyancy effects. Therefore the study of Rayleigh-Benard convection can help in understanding the circulation in atmosphere and assist in weather forecasting.

In the industrial context, Rayleigh-Benard convection has applications in electronic packaging, solar ponds, waste heat disposal systems and material processing such as solidification phenomena and crystal growth.

In the present work a Mach-Zehnder interferometer has been employed to collect the line-of-sight projections of the temperature field inside a Rayleigh-Benard setup. The geometry is circular in plan hence giving an axisymmetric configuration. The fluid employed is air. The line-of-sight projections of the temperature field have been collected in the form of interferograms.

1.1 Literature Review

Rayleigh-Benard convection problem has been studied extensively both theoretically and experimentally. The primary purpose has been the study of the flow

pattern in different geometrical configurations for a varied range of parameters. However, as far as flow in axisymmetric cavities is concerned, not much work has been published in the literature. Most literature in this area deals with the cavities that are either rectangular or square in plan. Apart from this, not many experimental studies have been reported.

1.1.1   Rayleigh-Benard Convection

A large amount of literature is available in the field of Rayleigh-Benard convection in rectangular cavities. One of the objective of the published research is to identify the critical Rayleigh number when flow undergoes a transition from one configuration to another. The critical Rayleigh number for the onset of convection in an infinite fluid layer does not depend on the Prandtl number of the fluid, whereas all subsequent transitions are strong functions of the Prandtl number. The critical Rayleigh number at the onset of convection is dependent on the geometry of the cavity. It decreases with the increasing aspect ratio. The aspect ratio is defined as the ratio of the horizontal width of the cavity to the vertical depth of the fluid layer. It is maximum for an infinite fluid layer.

When the Rayleigh number is very close to the critical value for the onset of convection, hexagonal cells have been observed both experimentally and numerically. Numerical studies have shown that for liquids, the fluid particles within the hexagonal cells have an upward motion in the center, while for gases the particles have a downward motion in the center.

For an increase in Rayleigh number, the formation of stable two dimensional longitudinal rolls are seen. The two dimensional rolls slowly deform to three dimensional rolls. For further increase in the Rayleigh number, adjacent rolls start to merge leading to a reduction in the number of rolls. The flow switches to a time-dependent regime at higher Rayleigh numbers and slowly approaches the turbulent state.

Experimental studies have shown that in an infinite fluid layer case the first transition from conduction to steady cellular convection occurs at a Rayleigh

number $Ra_{c_1} = 1707.8$ and this value is independent of the Prandtl number of the fluid considered. According to the theoretical work of Davis (1967) and Stork and Muller (1972), Ra_{c1} increases from 2×10^3 to 7×10^3 as the aspect ratio is decreased from 5 to 1. These results confirm the experimental works of Oertal (1976) and Catton (1970) which also show the same trend of behaviour of the first critical Rayleigh number as the aspect ratio is decreased from infinity.

Krishnamurti (1970) has given a diagram delineating the different transitions in a Rayleigh-Benard convection system as a function of Rayleigh number and Prandtl number. This is one of the earliest experimental studies where a number of different fluids were experimented with and a variety of cavity sizes were considered. For air (Pr=0.71), the author concludes that at about Ra=5000 the flow changes from steady two-dimensional to steady three- dimensional flow along with the loss of rolls. Around Ra=6000 the flow was observed to be time-dependent leading to turbulent state as the Rayleigh number was increased to Ra=10000.

The experiments of Gollub and Benson (1980) for small aspect ratio enclosures showed that the initial flow configuration consisted of two symmetric rolls in the steady state. This pattern was stable upto a certain value of the Rayleigh number. With the further increase in the Rayleigh number, the well- documented phenomenon namely the decrease in the number of rolls occurs. Mukutmoni and Yang (1992) numerically investigated the loss of rolls phenomenon in small box (4:2:1) for air. The transition from 4 to 3 rolls was observed with an increase in the Rayleigh number. The transition sequence showed the typical slanting of the rolls, as well as the thinning and thickening of the distorted rolls in the time sequence. Later, Mukutmoni and Yang (1994) showed that there is generation of vertical vorticity specifically a swirl in the transition process. For a small aspect ratio, Davis (1967) and Stork and Muller (1972) showed that only the rolls parallel to the shorter side of the container are stable, but according to Mukutmoni and Yang (1992) rolls parallel to the longer side for small box can be stable below a certain critical Rayleigh number. They concluded that the long rolls are metastable and are certainly less stable than the rolls parallel to the shorter side.

Michael and Yang (1992) have reconstructed the three dimensional temperature field from its interferometric projections and have seen the presence of rolls

in a water filled cavity of aspect ratios 8.7 and 9.0. The two horizontal confining walls of the cavity were made of aluminium. The top plate was cooled using constant temperature water flowing over the aluminium sheet. The bottom plate temperature was maintained using three electric foil heaters connected in series. Two sides of the vertical side walls were made from delrin and the other two sides were made from 25 mm thick optical flats. A Mach-Zehnder interferometer with 20 cm optics and a Helium-Neon laser of 10 mW power output were employed for collecting the projection data. Wedge fringe setting of the interferometer was used to record the convection pattern inside the cavity.

Muralidhar *et al.* (1996) have studied the transient convection in a two dimensional square cavity. The fluid considered was air. Rayleigh numbers in the range of 10^4 to 10^5 were employed. The cavity had a width of 74 cm and the aspect ratio considered was unity. The horizontal surfaces were developed using brass sheets. The vertical side walls employed were made of a low thermal conductivity material such as perspex. The isothermal conditions on the brass sheets were obtained by flowing water at constant temperature through them. A Mach-Zehnder interferometer was employed to map the thermal field. The experiments showed that the flow was mostly bicellular during the early transient period whereas it became unicellular at steady state. The Nusselt number in the cavity was found to be maximum at the steady state.

Forbes (1996) have reported a method for inverting the integrated phase-shift data obtained from an axisymmetric refractive index field. The method is based on the Onion Peeling Algorithm and determines the refractive index as a function of radius over a series of irregularly spaced, concentric rings whose edges correspond to the fringe location. This method is suitable for the analysis of axisymmetric interferograms.

Bhadra *et al.* (1997) studied the Rayleigh-Benard convection problem in a cylindrical axisymmetric geometry. The Rayleigh number employed was 6872 and diameter-to-height aspect ratio of the test cell was 36.1. A Mech-Zehnder interferometer was used to map the thermal field. The experiments were performed at steady state and the projections of the flow field were recorded at four different angles namely $0°$, $90°$, $180°$ and $270°$. The authors established the axisymmetric

nature of the flow field at steady state that was achieved after 4 to 5 hours from the start of the experiment. The final aim of the work was to reconstruct the three dimensional temperature field from its two dimensional projection data using standard tomographic algorithms.

Mishra *et al.* (1998) studied the problem of Rayleigh-Benard convection in intermediate aspect ratio enclosures with air as the working fluid. The Rayleigh number considered were 13900, 34800 and 40200. The authors concluded that at a Rayleigh number of 13900, the fringes were steady near the boundary walls but mild unsteadiness was present in the central horizontal layers. At the higher Rayleigh numbers of 34800 and 40200, the unsteadiness was more pronounced, with flow switching between two well-defined states. Apart from this study, the authors contributed notably in the field of tomography and developing a most versatile fringe thinning algorithm.

The construction of apparatus used for the study of flow and heat transfer in Rayleigh-Benard convection in the last two decades has been presented in a review paper by de Bruyn *et al.* (1996). Non-uniformities of the heat input to the two horizontal plates and the conductivity of the side walls are major concerns while making a convection test cell. In most of the experiments reported the top plate temperature was held fixed and the bottom plate temperature was controlled by varying the heat input. The experimentalists thus obtained the required temperature difference across the cavity. In most experiments the cooling of a surface was produced by passing water at a low temperature over the flat horizontal plates. The water temperature was kept constant using a heat removal device. For heating, some experiments used an electrical resistance supplied with an electrical input while others passed hot water over the surface. Uniformity and flatness of the two bounding surfaces was another issue where care had to be taken. Sagging of the horizontal surfaces was a frequently-faced problem.

1.2   Objectives of the Present Study

The present study is concerned with Rayleigh-Benard convection problem in an axisymmetric configuration. The cavity is circular with diameter of 64 cm and the vertical height of 2.3 cm. The working fluid is air. Four different Rayleigh numbers have been employed namely 6000, 8000, 10,000 and 12,000. The values of Rayleigh numbers have been calculated using Equation 1.1 and the fluid properties have been evaluated at the average cavity temperature in all the experiments conducted.

The present work is directed towards achieving the following objectives: (a) the influence of Rayleigh number on the steady state thermal field, (b) the transient evolution of the thermal field at a given Rayleigh number, (c) comparison of the convection patterns in axisymmetric fluid layers and cavities square in plan, (d) asymmetry of the thermal field in an axisymmetric geometry, and (e) comparison of the numerically generated solution of the flow and heat transfer problem.

The thermal field has been mapped using a Mach-Zehnder interferometer. The interferograms have been obtained as a collection of fringe patterns. The interferograms give line-averaged information along the direction of the light ray. Hence they represent a projection in that direction. The interferograms can be used to identify the flow pattern prevailing within the cavity.

Chapter 2

Apparatus and Instrumentation

A Rayleigh-Benard experimental setup is apparently simple in design. It comprises of two horizontal surfaces of high thermal conductivity which are maintained at different constant temperatures. The vertical side walls are perfect insulators. Though simple in design, various factors are taken into account during the fabrication of the test cell and also while experimentation. For example, uniformity and constancy of surface temperatures, parallelism of the walls defining the fluid layer and properties of the insulating surfaces are all factors that determine the quality of the experiments. Further, some extraneous factors such as building vibrations, air motion and changes in the ambient temperature strongly affect the recorded interferograms. Hence these experiments have to be performed with due care and precautions.

2.1   Test Cell for Rayleigh-Benard Convection

The apparatus used to study the convection phenomenon in the horizontal layer of fluid is shown schematically in Figure 2.1.

The test cell consists of three sections namely the **Top Tank, Middle Test Section** and **Bottom Tank**. The total tank diamter is 76 cm and the effective diameter of the fluid layer is 64 cm. The fluid layer was confined by two aluminium plates, 3 mm thickness above and below. The flatness of these plates was carefully

established against a reference face plate and a ground flatness to within ± 1 mm was achieved through continous effort. Both surfaces were maintained at uniform temperatures by circulating a large volume of water over them.
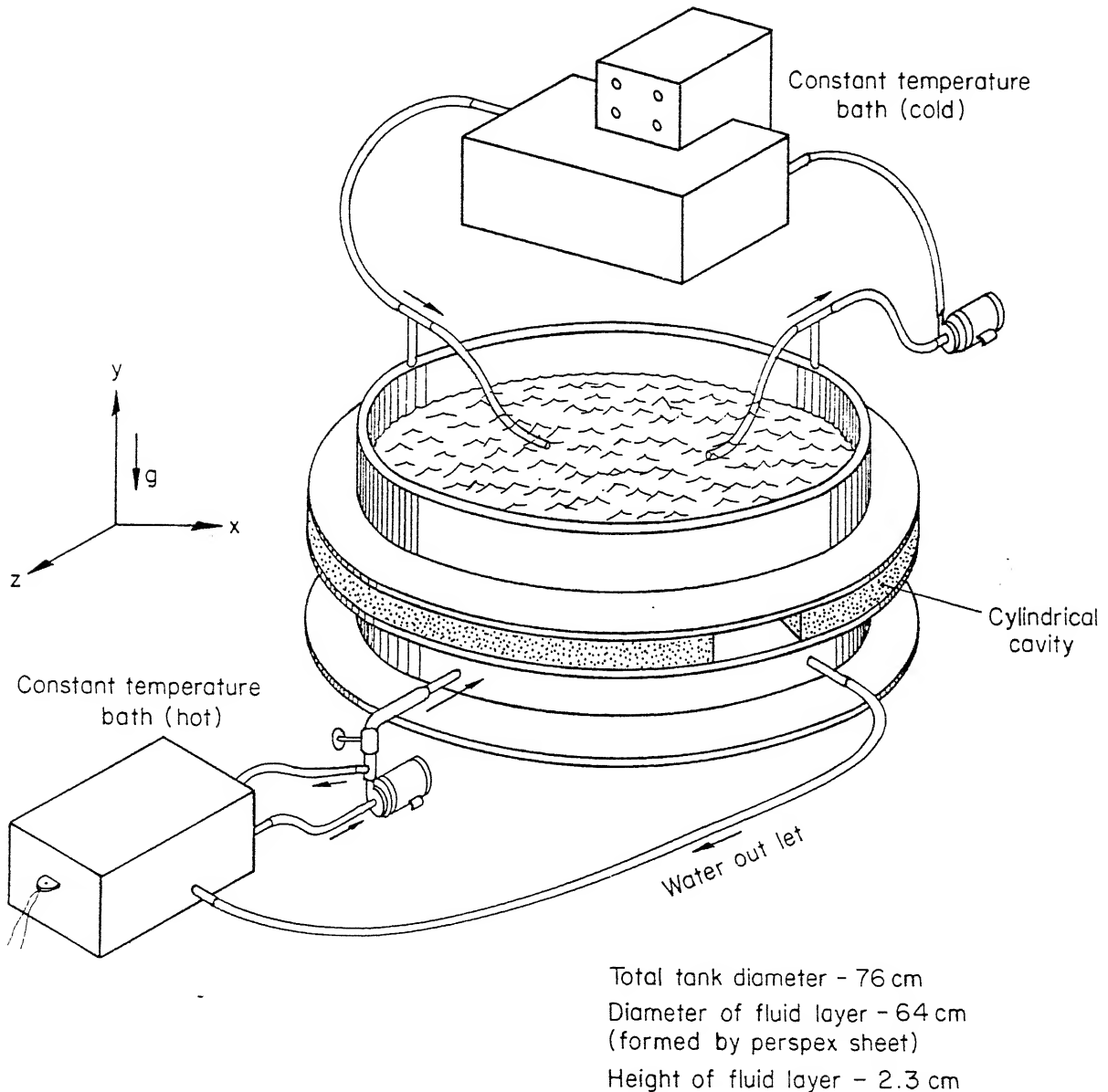

Figure 2.1: Schematic Drawing of the Apparatus for Rayleigh-Benard Convection

For the upper plate, a tank-like construction enabled extended contact between the flowing water and the aluminium surface. Water was circulated from a constant temperature bath which was maintained at a lower temperature as compared to the temperature of water that was circulated in the lower tank. Enough precautions were taken so as to avoid the leakage of water from the joints. The top plate was strong enough not to slack down due to the weight of water. The tubes through which water circulated were completely submerged in the upper tank in order to avoid the formation of air bubbles which could have disturbed the flow rate. The constant temperature bath has the maximum force pump capacity of 10 litres/min and maximum suction pump capacity of 7 litres/min . Temperature adjustments and temperature indications are digital. The operating temperature range is $-30°C$ to $150°C$.

Water in the lower tank of the experimental test cell was circulated from a water tank by means of a pump. Special arrangements were required to maintain contact between water and the lower surface of the plate. The flow of water below the lower surface was pressurized and the presence of baffles introduced a tortuous path, thus increasing the effective interfacial contact area. The tank was sufficiently sealed with screws and rubber sheet to prevent a leak. The circulating water was maintained at room temperature in all the experiments. The interfacial contact between the lower surface of the plate and water ensured a uniform temperature through out the surface of the lower plate. This was cross checked by measuring the temperatures at various points on the surface and the maximum variation was within $±0.1°C$ over the entire surface.

The middle section of the experimental test cell is the test section that contains the fluid whose convection pattern is to be studied. The side walls that define this section comprised of perspex sheets. The perspex sheets were surrounded by a thick rubber padding and foam in order to insulate the test section from the outside atmosphere. Perspex sheets, rubber padding and foam also supported the weight of the upper tank. The perspex sheets were well in contact with the upper and lower plates. To take extra precautions, a thin layer of cloth was applied on the top of the perspex sheets so as to fill the minor gaps between the top plate and perspex sheets. Giving a perfect circular shape

to the perspex sheets requires tremendous effort during the fabrication of the entire test cell. These sheets were bent in circular shape to a diameter of 64 cm and this is the effective diameter of the test section. This diameter was kept uniform in order to ensure the axisymmetric configuration of the test cell, the main objective of the present study. The height of the test section was 2.3 cm and was uniform to within ± 0.1 mm. A provision was made to accommodate a small window in the perspex side wall for the recording of the interferograms. During the experiments, the windows were closed so that contact with the outside atmosphere was prevented. The protruding portion of the upper and the lower plates near the windows was filled with foam in order to avoid the formation of convection currents in that region that could have interfered with the patterns inside the cavity while recording the interferograms.

2.2   Traversing Mechanism

A traversing mechanism is needed to mount the apparatus in which the desired experiment is in progress. In practice, the optics and the laser source cannot be moved to scan the flow field. The traversing mechanism enables translation and rotation of the test cell. The traversing mechanism is schematically shown in Figure 2.2.

The base of the traversing mechanism is padded with a rubber sheet of 30 mm thickness to damp any external vibration from reaching the test cell.

Enough precautions were taken to ensure that the convection patterns in the fluid layer were insensitive to external disturbances such as floor vibrations and atmospheric air currents. The entire test cell was placed inside a chamber made of a plastic-sheet to eliminate the influence of external air currents. The ground vibrations were eliminated by placing the interferometer over four pneumatic isolation mounts. Once the mounts are pressurized the entire interferometer floats over these mounts.

180   90   270   0

LASER

1. Mount for apparatus
2. Base plate
3. Lead screw
4. Bearings support
5. Outer frame
6. Scale

120 cm

80 cm

70 cm
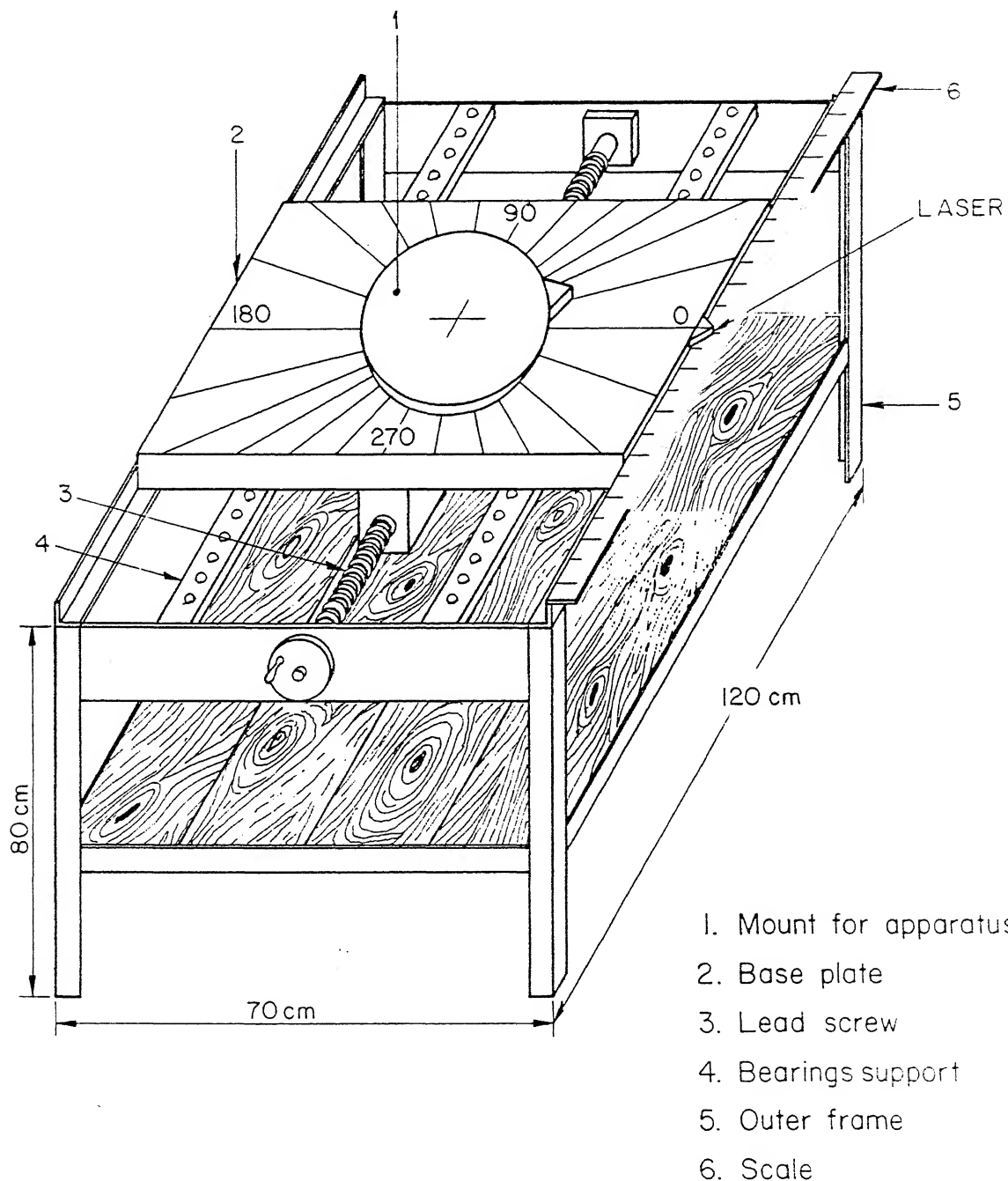
Figure 2.2: Schematic of the Traversing Mechanism

2.3   Mach-Zehnder Interferometer

A Mach-Zehnder interferometer has been used in the present study to visualise the convection patterns in the fluid layer. Figure 2.3 shows the schematic diagram of the Mach-Zehnder interferometer.
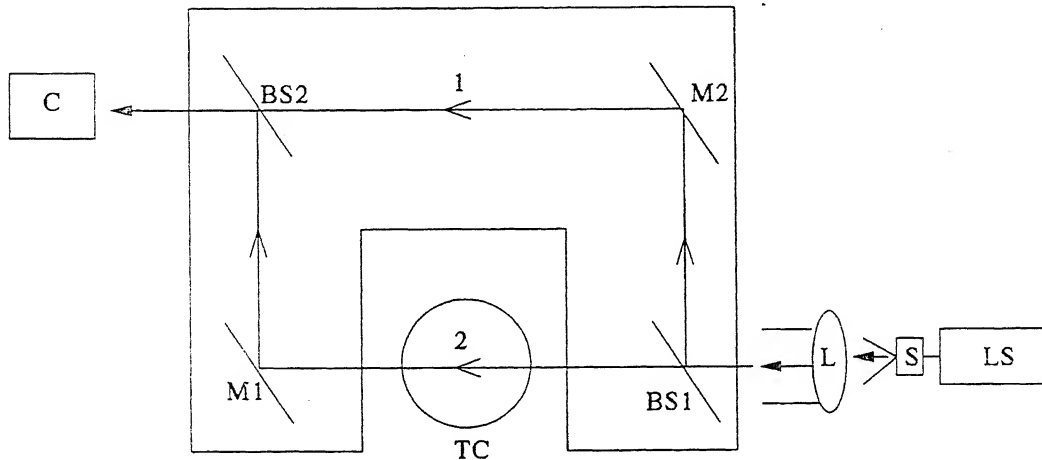
M	Mirror	L	Convex lens	1	Reference beam
BS	Beam splitter	LS	Laser source	2	Test beam
C	CCD camera	S	Spatial filter		

Figure 2.3: Schematic Drawing of the Mach-Zehnder Interferometer

The optical components present in it namely the beam splitters BS1 and BS2 and mirrors M1 and M2, are inclined exactly at an angle of $45°$ with respect to the laser beam direction. The first beam splitter BS1 splits the incoming collimated beam into two equal parts, transmitted and the reflected beams. The transmitted beam (2) is labelled as the test beam and the reflected beam (1) as the reference beam. The test beam passes through the test region where the convection process is in progress. It is reflected by the mirror M1 and recombines

reference beam on the plane of the second beam splitter (BS2). The reference beam undergoes a reflection at mirror M2 and passes through the reference medium unaltered and is superimposed with the test beam at BS2. The two beams on superposition at second beam splitter BS2, produce an interference pattern. This pattern contains the information of the variation of the refractive index in the test cell. For measurements in air, the reference medium is simply the ambient. The optics employed in the present configuration are of 150 mm diameter. The beam splitter has 50% reflectivity and 50% transmitivity. The mirrors are coated with 99.9% pure silver and employ a silicon dioxide layer as a protective layer against oxidation.

The Mach-Zehnder interferometer can be operated in two modes; namely (a) Infinite fringe setting and (b) Wedge fringe setting. In (a) the test and reference beams are set to have identical geometrical path lengths and fringes form due to density and temperature changes alone. Since each fringe is a line of constant phase, it is also a line of constant refractive index, a line of constant density and hence temperature and hence an isotherm. The infinite fringe setting is employed for high accuracy temperature measurements in the fluid. In (b), the mirrors and beam splitters are deliberately misaligned to produce an initial fringe pattern of straight lines. When a thermal disturbance is introduced in the path of the test beam, these lines deform and represent temperature profiles in the fluid. The wedge fringe setting is commonly employed for heat flux measurements.

2.3.1   Laser Source

A 35 mW, continous wave (632.8 nm) He-Ne laser is employed as the coherent light source for the interferometer. The original laser beam is of 2 mm diameter, therefore a spatial filter is required to expand the laser beam to any convenient diameter. In the present work the laser beam is expanded to 70 mm diameter and a plano convex lens is used to collimate the beam.

2.3.2 ‸ CCD Camera

A CCD (Charge Coupled Device) camera of spatial resolution of 512×512 pixels has been used to capture the interferometric images. This camera is connected to a PC-based image processing system through an 8-bit A/D card. The fringe pattern is stored in the form of a matrix of integers, with intensities varying between 0 and 255, where 0 indicates black and 255 the complete white. In the present setup the image acquisition is at video rate, namely 50 images per second.

2.4   Alignment of the Interferometer

Before the start of the experiment the interferometer has to be aligned. All the experiments in the present work are performed with the infinite fringe setting mode of the interferometer. Adjustment of the infinite fringe setting is delicate and requires efforts. The initial field of view is one of complete brightness since the interference is constructive. The geometrical and the optical path lengths of the test and reference beams are same in the absence of any thermal disturbances in the path of the test beam. As the interferometer approaches the infinite fringe setting the distance between the fringes increases and the number of fringes decreases. Figure 2.4 shows the infinite fringe setting mode of the interferometer.

Figure 2.4: Infinite Fringe Setting of the Interferometer

The wedge fringe setting is comparitively easier to set up than the infinite fringe setting. Here the initial fringes form due to deliberate misalignment between the optical components. The orientation of the fringes can be changed by adjusting

the inclination of the optical components. Figure 2.5 shows the wedge fringe setting mode of the interferometer.
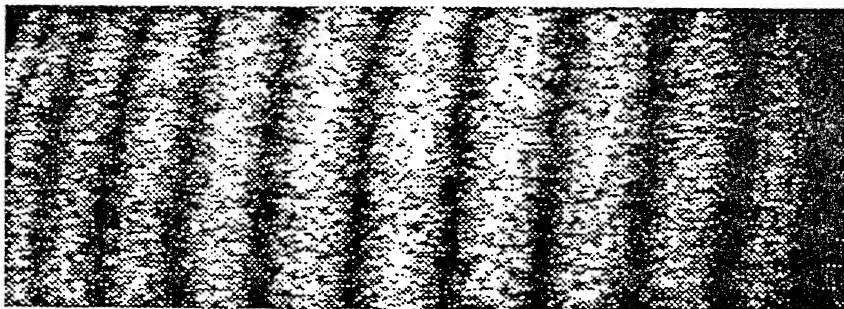

Figure 2.5: Wedge Fringe Setting of the Interferometer

2.5   Experimental Procedure

Before the start of the experiments, the Mach-Zehnder interferometer is set in the infinite fringe setting mode. The interferometer lies on the pressurised pneumatic isolation mounts and this ensures that the floor vibrations and other external disturbances do not disturb the initial setting of the interferometer. A cross-check is again made after sometime in order to ensure that the infinite fringe setting in fact prevails in the experiment and after that only the experiment is started. All the experiments have been performed to record the long-time convection patterns prevailing in the test cavity so that the steady state is reached before recording the interferograms. The experiments are run for a period of 11 to 12 hours at an stretch to achieve this condition.

Isothermal conditions on the lower and the upper plates of the test cell are ensured by circulating a large volume of water in the lower and the upper tank. Temperature measurements are made at regular intervals of time during the experiments. Total experimental run time of around 12 hours enables the plates to acquire a constant and uniform temperature through out their surfaces and hence leading to isothermal conditions. The whole test cell is placed inside a plastic sheet chamber to avoid the effects of external air currents.

The interferograms have been recorded at regular intervals of time in order

to show the transients that the fluid undergoes before reaching the steady state. At steady state, three to four interferograms have been recorded in a gap of 10 to 15 minutes to ensure that the steady state condition in-fact prevails in the cavity. At the time of recording of these interferograms, the cover of the windows are taken out gently and placed back once the recording is over. In order to prove the axisymmetric nature of the flow field prevailing in the test cavity, the experiments have been performed at different angles by rotating the test cell. In all the experiments the position of the CCD camera is fixed. The lights of the room are switched-off at the time of recording of the interferograms .

The complete view of the experimental setup with all the accessories are shown in Figure 2.6 and Figure 2.7 shows the closer view of the axisymmetric test cell used to study the convection patterns of the fluid layer.
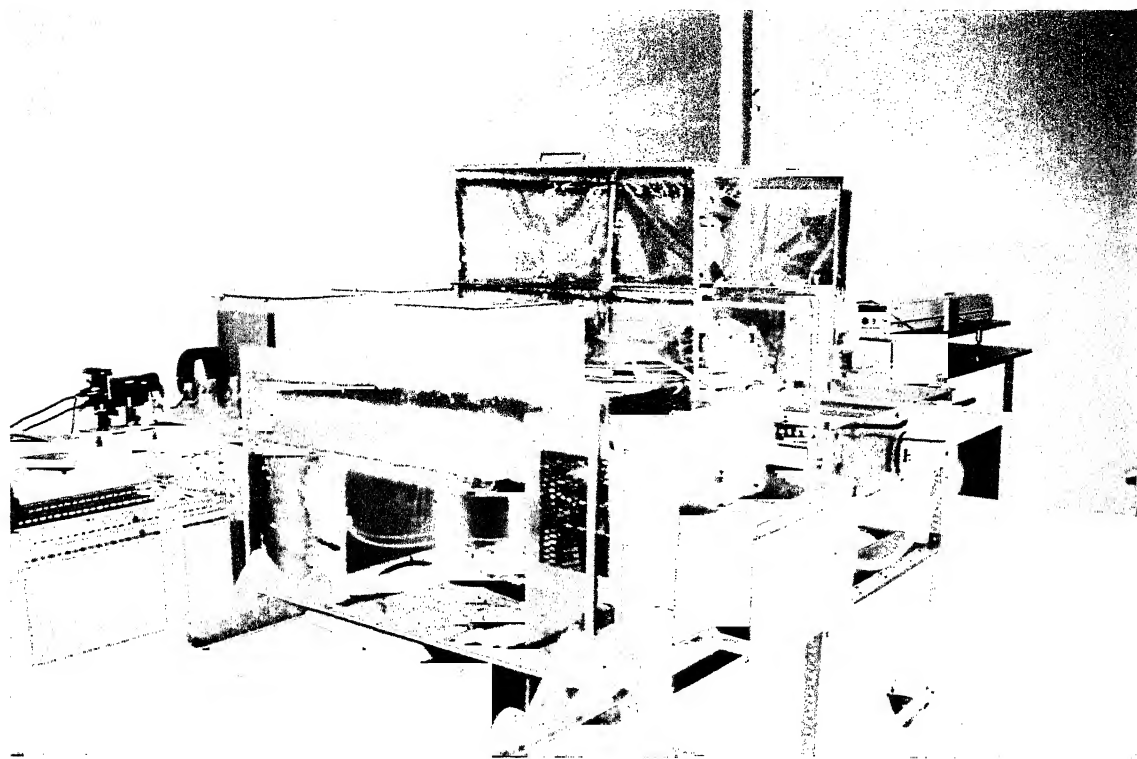
Figure 2.6: Complete View of the Experimental Setup
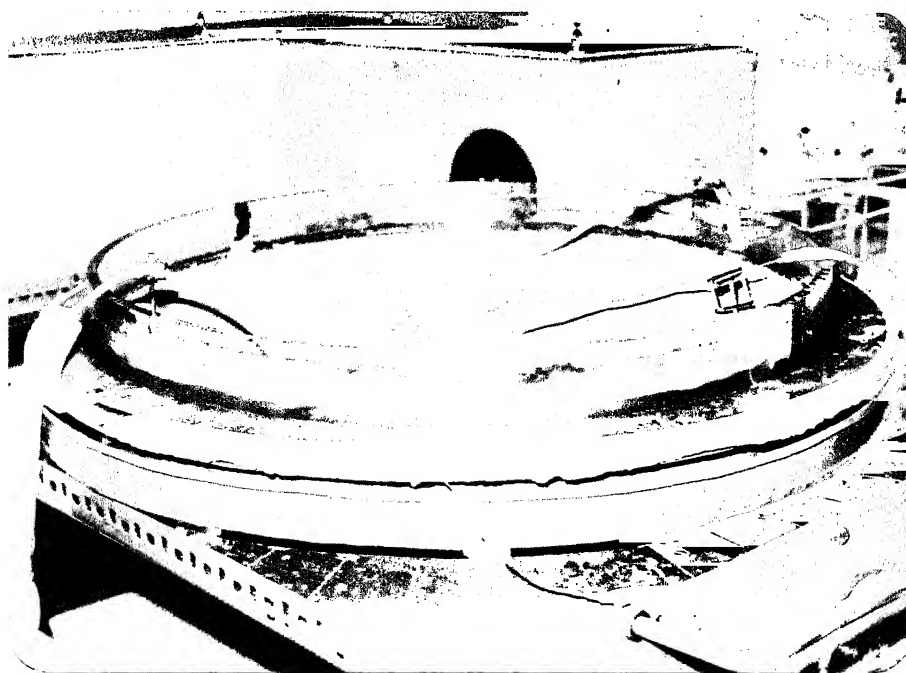
Figure 2.7: Closer View of the Test Cell

Chapter 3

Data Reduction

Optical techniques employed in fluid-flow measurements can be classified into three categories: (i)direct flow visualisation by injecting some tracer particles (e.g. dyes, bubbles, solid particles), (ii) laser-doppler systems where the frequency shift of scattered illumination from an injected tracer medium in the flow field is measured and (iii) measurement of index of refraction of the fluid or its spatial derivatives. Three popular methods that fall into the third category are:

1. **Shadowgraph**, measures the variation of the second order derivative of the index of refraction normal to the light beam. The focus is on the reduction in light intensity as the beam diverges.

2. **Schlieren**, handles the variation of first order derivative if the index of refraction normal to the light beam. Here the deflection of light in a variable refractive index field is captured.

3. **Interferometry**, responds directly to the refractive index field of the flow system. Here the image formation is related to changes in the refractive index with respect to a reference environment.

This chapter discusses the principles of interferometry and procedures for the evaluation of the interferograms. The concepts of interferometry with reference to temperature field in the infinite fringe setting of Mach-Zehnder interferometer

have been discussed. Apart from these features this chapter also discusses the techniques used to improve the image quality and fringe thinning techniques.

3.1 Interferometry

As discussed, in interferometry, the image formation is related to the changes in the refractive index of the fluid with respect to the reference environment. In the present work, attention is restricted to the image patterns that form in the infinite fringe setting mode of the interferometer. When isothermal conditions prevail in the test beam path each ray of light undergoes a change of phase, depending on the extent of change of the refractive index of the medium. Hence an optical path difference is established between the test and the reference beams, resulting in a fringe pattern. For temperature measurements, the refractive index variation has to be related to that of temperature.

For gases, the relationship

$$\frac{n-1}{\rho} = \text{constant} \tag{3.1}$$

holds good, where ρ is the density of the fluid. This relationship is called the Gladstone-Dale equation (Goldstein, 1983). It follows that $dn/d\rho$=constant. Now for moderate changes in temperature, density vaties linearly with temperature as

$$\rho = \rho_0(1 - \beta(T - T_0)) \tag{3.2}$$

Hence dn/dT is also a constant. This implies that changes in temperature simultaneously result in changes in refractive index and this leads to changes in the phase of the wave. This is the origin of fringe formation in interferometry.

Let $n(r, z)$ and $T(r, z)$ be the refractive index and temperature fields respectively in the test region and n_0 and T_0 be the reference values of n and T respectively as encountered by the reference beam. Let L be the geometrical path length covered by the test and reference beams. Now for the test beam, the optical path length is defined as

$$PL = \int_0^L (n(r, z))ds \tag{3.3}$$

and for the reference beam,

$$PL = \int_0^L (n_0)) ds \tag{3.4}$$

is the optical path length. The interferogram is a fringe pattern arising from the optical path difference

$$\Delta PL = \int_0^L (n(r,z) - n_0) ds \tag{3.5}$$

which in terms of temperature is

$$\Delta PL = \frac{dn}{dT} \int_0^L (T(r,z) - T_0) ds \tag{3.6}$$

The integral is evaluated along the path of a light ray given by the coordinate s. The fringes seen on the interferograms are locus of points having the same optical path difference. Hence on any given fringe the optical path difference ΔPL is a constant and

$$\int_0^L (T(r,z) - T_0) ds = \frac{\Delta PL}{dn/dT} = \text{constant}$$

Hence

$$\int_0^L T(r,z) ds - T_0 L = \text{constant}$$

The integral $\int_0^L T(r,z) ds$ is defined as $\overline{T} L$, where $\overline{T}$ is the average value of $T(r,z)$ over the length L of the laser beam through the test cell. This is also the line integral of the function $T(r,z)$. Hence

$$L(\overline{T} - T_0) = \text{constant} \tag{3.7}$$

In the infinite fringe setting Equation 3.7 holds good for all the fringes. Now since the dimensions of the windows through which the laser beam is allowed to pass are very small as compared to the overall dimensions of the test cell (the window width is 5.5 cm and the diameter of the test cavity is 64.0 cm), it can be assumed that, for an interferogram, curvature effects are unimportant and L is constant for all the rays. With this assumption, Equation 3.7 implies that $\overline{T}$ is a constant over the fringe. Hence each fringe represents a locus of points over which the average of the temperature field along the direction of the ray is a constant, hence fringes are isotherms.

Defining the function $L(\overline{T} - T_0)$ in Equation 3.7 as $f(\overline{T}, L)$, the fringe temperature on two successive fringes for same value of L can be given as :

$$\text{fringe 1:} \quad f_1(\overline{T}, L) = \frac{\Delta PL}{dn/dT}$$

$$\text{fringe 2:} \quad f_2(\overline{T}, L) = \frac{(\lambda + \Delta PL)}{dn/dT}$$

where λ is the wavelength of the laser used. From these two equations, the temperature drop per fringe shift, ΔT_ϵ, can be calculated as

$$\Delta T_\epsilon = \frac{1}{L}\left(f_2(\overline{T}, L) - f_1(\overline{T}, L)\right) = \frac{\lambda/L}{dn/dT} \tag{3.8}$$

3.2 Image Enhancement

The images of the fringe pattern collected using the CCD camera and the A/D card are tend to be noisy. Noise can be defined as extraneous and unwanted intensity variation which is superimposed over the useful portion of the data. There are various factors that are responsible for the generation of noise in the recorded data like imperfection of the optical components, noise in the CCD array, digitization process etc. However, the most dominant factor is speckle which is the major source of noise in the interferometric images. Speckle is a superposition of diffraction patterns over the basic interference pattern . It arises from the imperfection of the optical surfaces. The presence of microscopic unevenness on the optical surfaces leads to diffraction. The diffracted rays interfere and generate local fringe patterns and corrupt the global intensity distribution. Filtering is required to extract the original intensity information from the recorded interferogram which is then processed for contrast improvement.

3.2.1 Filtering

Fourier filtering method has been used to extract the useful information from the recorded interferograms. Figure 3.1 shows the original interferogram as recorded

from the interferometer.

Figure 3.1: An Original Interferogram

For Fourier filtering the image is first transformed to the wavenumber space with a two dimensional Fourier transform operation. The wavenumber is a kind of a spatial frequency and is defined as the number of intensity cycles per pixel. Intuitively one can view the low wavenumber harmonics as information and high wavenumber harmonics as noise. Now in the wavenumber domain, a two-dimensional band pass filter can be used to effectively set the high wavenumber components to zero. An inverse Fourier transform restores the filtered image in the spatial domain. Figure 3.2 shows the filtered interferogram of the same image as shown in Figure 3.1.
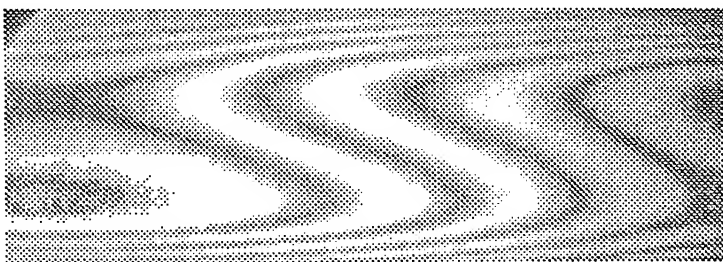
Figure 3.2: Filtered Interferogram

3.2.2   Contrast Improvemnet

As mentioned in the previous section, filtering removes the high wavenumber components of the intensity distribution and thereby removes the unwanted noise in the image data. At the same time, the image becomes blurred owing to the loss

of contrast. Since the visual appearance of the original interferogram as recorded
through the CCD camera is not good (as seen from Figure 3.1)), the Fourier
filtering operation further leads to the loss of the contrast. Hence there is a need
for contrast improvement of the image that has to be analysed. Different contrast
improvement software packages are available through which one can enhance the
quality of the image. Examples are GIMP, Electric Eyes etc. In the present
work, Electric Eyes software has been used for this purpose. Figure 3.3 shows the
contrast improved image of the same interferogram as shown on Figures 3.1 and
3.2. There is a definite improvement in the visual appearance of the image and
the fringes are now more clearly visible.
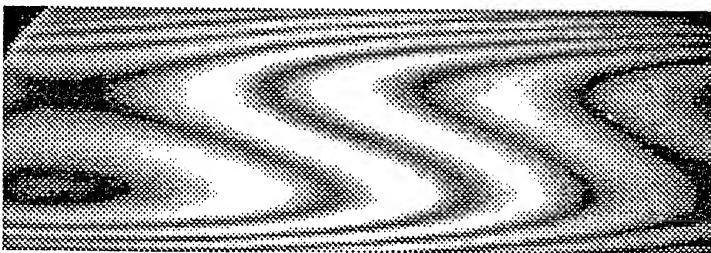
Figure 3.3: Contrast Improved Interferogram

3.3   Fringe Thinning

In the interferometric images, the fringes are represented by the alternate dark
and bright bands. The quantitative information, temperature in the present work,
is thus spread over the whole width of these bands that constitute the fringes.
Hence fringe thinning is one of the most important operation in the extraction
of quantitative information from the collected interferograms. It is the process of
extraction of the set of points of minimum or maximum intensities in the dark and
bright bands of the fringes. The minimum intensity corresponds to the points of
complete destructive interference and hence will have a zero intensity. Similarly,
a maximum intensity will appear at the points of constructive interference. In
the present work, the fringe bands are reduced to fringe curves by locating the
intensity minima in the dark fringe bands.

Automatic Fringe Thinning Algorithm (Mishra *et al.*), (1998) has ben applied in the present work in order to reduce the fringe bands into fringe skeleton or curves. It consists of tracing of the fringes in the direction of minimum intensity within an interferogram. The method is referred as automatic owing to the fact that once the single point is specified, the algorithm does not require user's intervention while the tracing is in progress. All the method requires is the starting point for each fringe and after that it is totally automatic.

Figure 3.4 shows the superposition of the fringe skeleton and the interferogram while Figure 3.5 shows the thinned image developed using the above mentioned fringe thinning algorithm.

Figure 3.4: Superimposed Thinned Image with Original Image
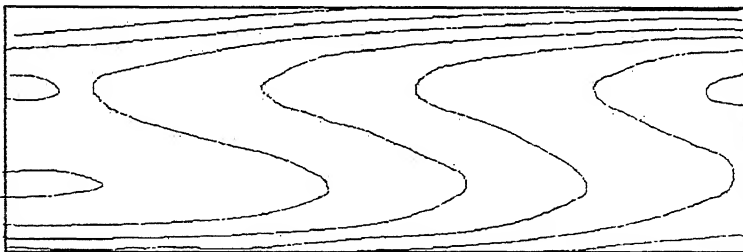
Figure 3.5: Thinned Image

3.4 Calculation of Fringe Temperatures

The calculation of temperature associated with the fringes is the most important step in interferometry. Figure 3.6 shows the schematic of a fringe skeleton after

thinning. The upper and lower walls shown in the figure have known temperatures. Near the walls. a high temperature gradient results in a large number of thin fringes which are very closely spaced. Due to the finite resolution of the CCD camera, it may be possible that a few number of fringes near the walls could be lost during the recording of the interferograms. Hence the first fringe seen on the interferogram near the wall will be of some arbitrary order. Therefore one cannot assign a temperature to the fringes directly using the value of tempreature difference per fringe shift though the wall itself is an isotherm.
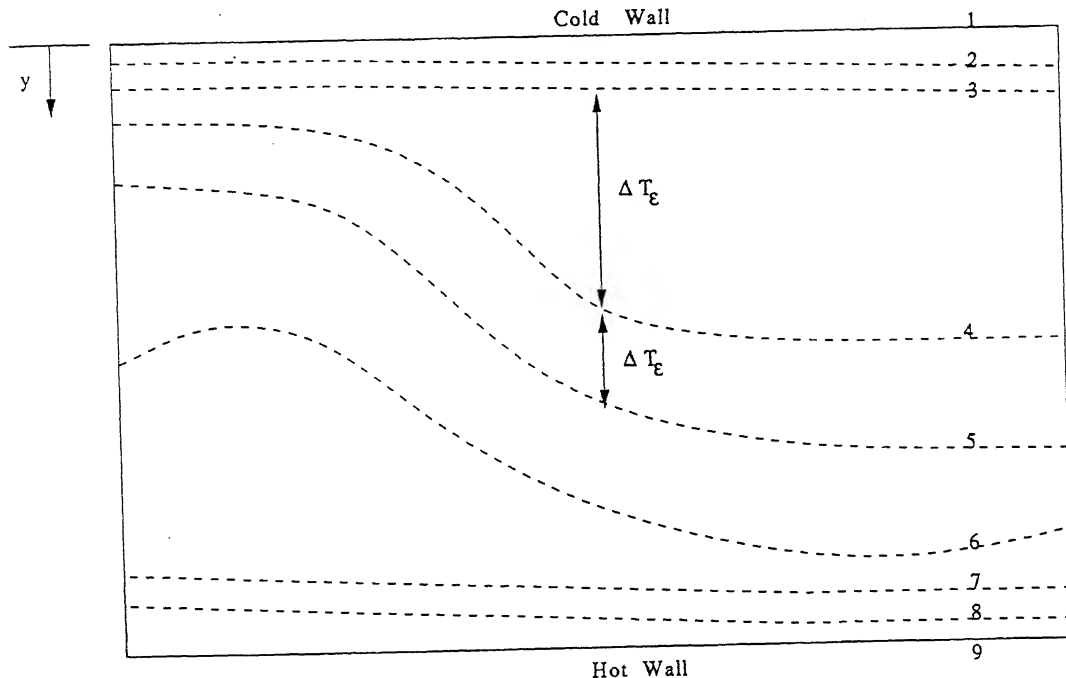
Figure 3.6: Schematic of an Idealized Fringe Skeleton for Temperature Calculations

Consider the fringes marked 2,3,4 in Figure 3.6. Fitting a function of type

$$T(y) = a + by + cy^2 \tag{3.9}$$

where y is a vertical coordinate, we get

$$\Delta T_\epsilon = T_2 - T_3 = b(y_2 - y_3) + c(y_2^2 - y_3^2) \tag{3.10}$$

$$\Delta T_\epsilon = T_3 - T_4 = b(y_3 - y_4) + c(y_3^2 - y_4^2) \tag{3.11}$$

These two equations are solved for the constants b and c.

The local wall temperature is $(\partial T/\partial y)_{y=y_1}$ and using equation 3.9, this can be expressed as $(b + 2cy_1)$. Similarly, the gradient in temperature field at the

first fringe is $(b + 2cy_2)$. Now the average of these two gradients is taken and is alloted as the wall temperature gradient. Finally, once this is known, the first fringe temperature near the top wall is calculated as

$$T_2 = (y_2 - y_1)\frac{(b + 2cy_1) + (b + 2cy_2)}{0.5} + T_1 \qquad (3.12)$$

The subsequent fringe temperatures are found out by simply adding ΔT_ϵ , the temperature difference per fringe shift, to the temperature of the previous fringe when started from the upper wall. In the present work, these temperature calculations were carried along a particular column and the column was selected where the near wall fringes are dense.

3.5 Nusselt Number Calculations

Nusselt number calculations have been used to determine the heat transfer rates at the boundary walls of the cavity and is defined as

$$\text{Nu} = \frac{-h}{T_{hot} - T_{cold}} \frac{\partial T}{\partial y} \big|_{y=0,h} \qquad (3.13)$$

In the present work average nusselt number at the top and the bottom walls have been reported. The average Nusselt number for each of the plates has also been compared with the experimental correlation reported by Gebhart *et al.* (1998) . For air, the correlation is given by:

$$\text{Nu} = 1 + 1.44\left[1 - \frac{1708}{\text{Ra}}\right] + \left[\left(\frac{\text{Ra}}{5830}\right)^{1/3} - 1\right] \qquad (3.14)$$

The Nusselt number calculations have been performed for one Rayleigh number namely Ra=12,000 at 0° projection angle and is compared with the reference value as given by the above mentioned correlation.

Chapter 4

Results and Discussion

The experiments in the present work have been performed at four Rayleigh numbers namely 6000, 8000, 10,000 and 12,000. In order to test the axisymmetric nature of the flow field, interferograms have been collected from three projection angles $0°$, $45°$ and $90°$.

The present chapter discusses various qualitative and quantitative issues related to the evolution of the flow field. Flow structures and roll pattern, transient evolution of the flow field and steady state nature of the flow field for all the four Rayleigh numbers have been reported. In order to demonstrate the axisymmetric nature of the flow field, the interferograms collected from three different projection angles have been presented for all the four Rayleigh numbers. For Ra=12,000, fringe temperature calculations, average Nusselt number over the top and the lower walls and temperature variation with the height of the cavity have been reported in the chapter.

In the series of experiments, the size of the cavity is quite large, and the fluid layer remains in this transient state for a considerable amount of time till it realizes the effect of circular boundary walls. In the early stages of the experiments, the fringe patterns of the square cavity are seen to be reproduced for shorter times. The fringe pattern for a square cavity are shown in Figure 4.1.

It has been observed that the planform of the convection pattern in the test cavity strongly depends on the shape of the boundaries of the fluid layer.
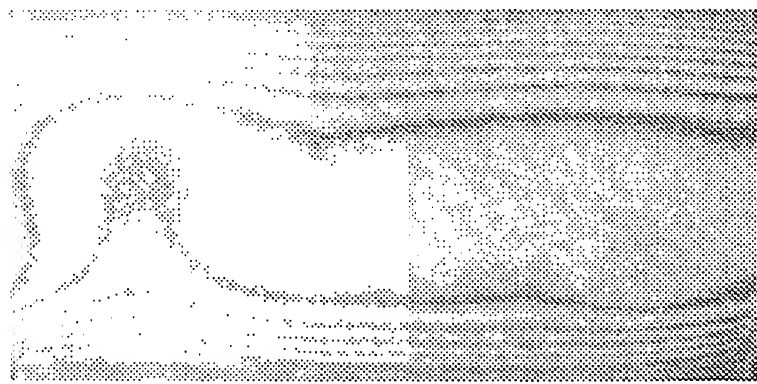
Figure 4.1: Steady State Fringe Pattern in Square Cavity

In a rectangular cavity, the roll formation is parallel to the shorter side. In an axisymmetric geometry the rolls are possibly in the form of concentric rings. These possible roll formation in a rectangular and axisymmetric geometry have are shown in Figures 4.2 and 4.3 respectively.
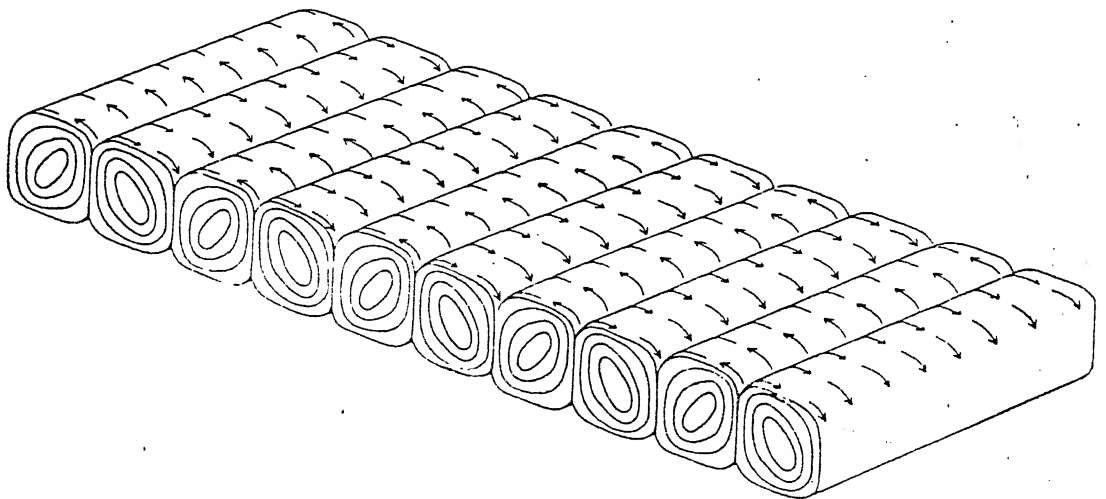
Figure 4.2: Roll Formation in a Rectangular Cavity
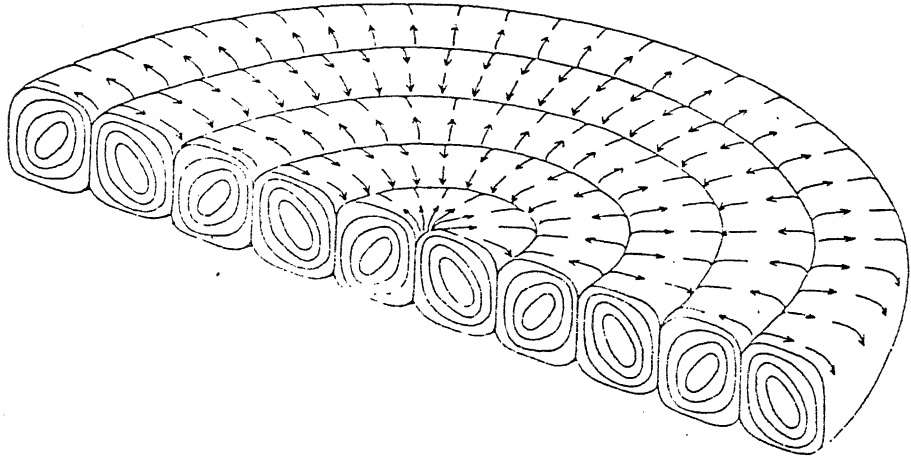
Figure 4.3: Roll Formation in an Axisymmetric Geometry

In order to validate the experimental results, a numerical simulation has been carried out for the flows in axisymmetric geometry. The Rayleigh number considered is Ra=6000. The governing equations, initial and boundary conditions and the numerical technique used along with the results obtained have been discussed in the Appendix.

4.1 Convection at Ra=6000

The experiments with Ra=6000 have been considered first. The intergerograms were recorded from three different projection angles namely 0°, 45° and 90° to establish the axisymmetric nature of the fluid layer. For a particular view angle, the transient evolution of the flow field have been recorded at regular time intevals till the steady state is reached.

4.1.1   Transient Evolution of the Flow field

Figure 4.4 shows the transient evolution of the thermal field till the steady state is reached. The interferograms were collected in regular intervals of time as shown. Initially the flow field consists of nearly straight fringes when the convection has just started, Figure 4.4(a). The fringes are closer and parallel to the boundaries which indicates that convection in the test section has not been established. The heat transfer is between the fluid and the surface, but not between the surfaces themselves. With the passage of time , the fringes are no longer straight, having a small amplitude deviation which is wavy in appearance, Figure 4.4(b) and Figure 4.4(c). The isotherm spacings near the top and bottom walls of the cavity is less than the spacing in the central region of the test section. This is expected, because near the boundaries heat transfer rates are higher; in the central region of the test section, heat transfer is practically absent. The flow field is in transient state with the fringes deforming from straight to curved shapes as seen from Figure 4.4(d) to Figure 4.4(f).

In the present experiment with an axisymmetric configuration, the transient evolution of the thermal field took place over a substantially longer time scale (for about 10 hours) compared to a square cavity. Mishra *et al.* (1998) have reported a time scale of 4-5 hours in their experiments. Once the flow field has fully evolved, the fringe patterns were observed to be quite steady without any sideways movement of the fringes, the phenomenon which was observed for higher Rayleigh numbers. Figure 4.4(g) and Figure 4.4(h) show the steady state nature of the flow field. These interferograms were recorded after 11 hours of the experimental run time to ensure the steady state behaviour of the convection pattern.
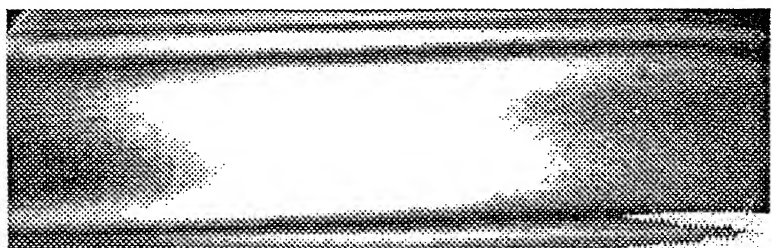
Fig.4.4(a)   1hour
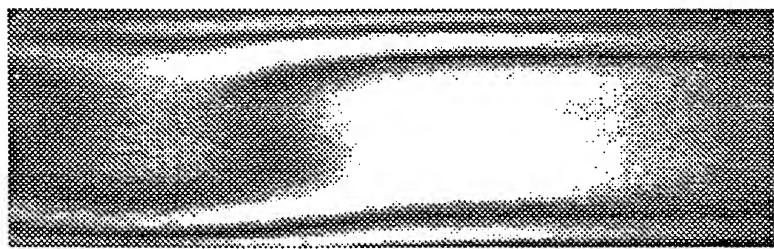
Fig.4.4(b)   2hours

Fig.4.4(c)   2hours 30min

For Caption see next page
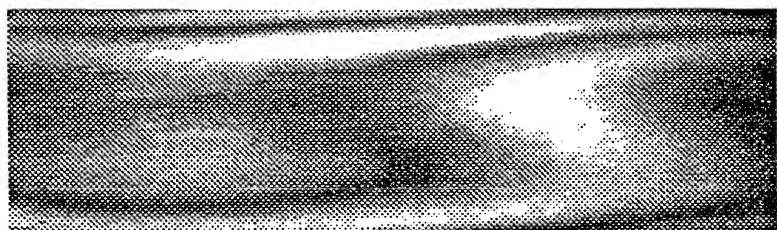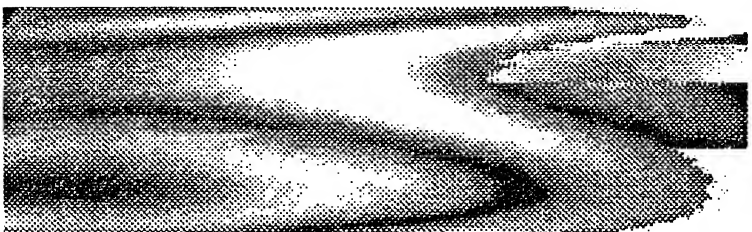
Fig.4.4(d)   5hours
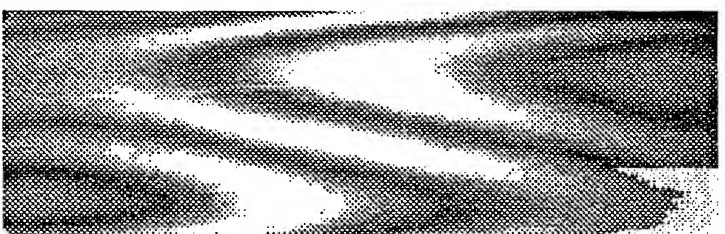
Fig.4.4(e)   7hours 15min
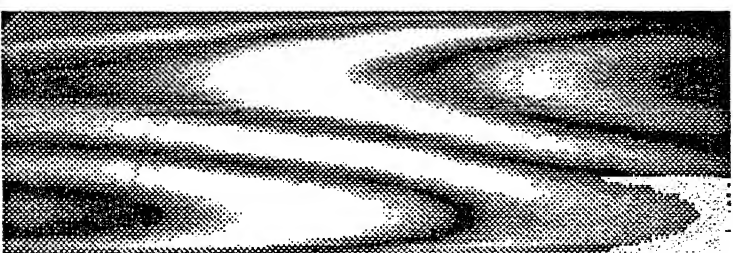
Fig.4.4(f)   9hours 30min

For Caption see next page
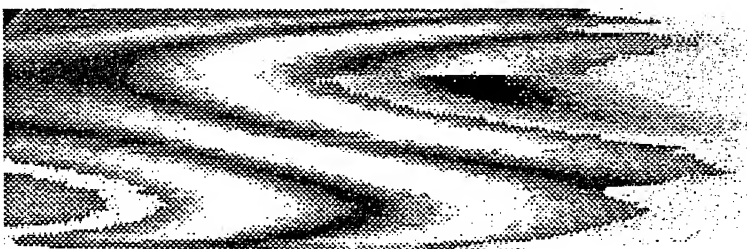
Fig.4.4(g)   9hours 45min

Fig.4.4(h)   11hours

Figure 4.4: Pattern Evolution for Ra=6000

4.1.2   Axisymmetry of the Flow field

The interferograms were collected from three different view angles namely 0°, 45° and 90°. Figure 4.5 shows the steady state patterns of the flow field for these three angles. All the three recorded interferograms appear to be identical and the number of friges in each interferogram is same. Also the respective fringe spacings are almost equal for each image. This establishes the axisymmetric nature of convection in the fluid layer at this Rayleigh number though variations can be seen within each image.

At steady state, the variation of the temperature field plotted as a function of the vertical distance is shown in Figure 4.6. Figure shows the temperature variation for equally spaced columns along the width of the cavity.

Figure 4.7 shows the variation of the line integrals of the temperature field averaged over a horizontal plane as a function of the vertical coordinate. The line integrals are simply the temperatures as computed from the interferograms. The y coordinate is measured from the cold top wall. The S-shaped curve which is the characterestic of the buoyancy driven convection phenomenon can be seen in all the plots. The slopes of the curves at the top and the bottom walls are practically equal supporting the fact that the net energy transfer across the cavity is a constant as we move from the lower hot wall to the upper cold wall.

0°

45°
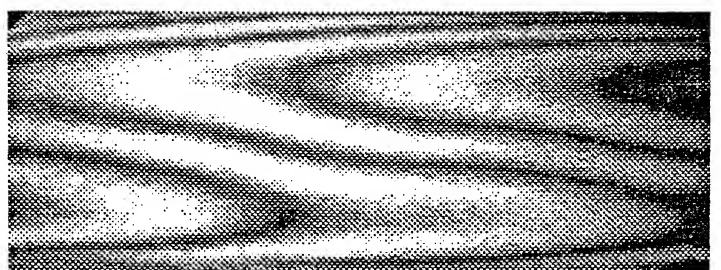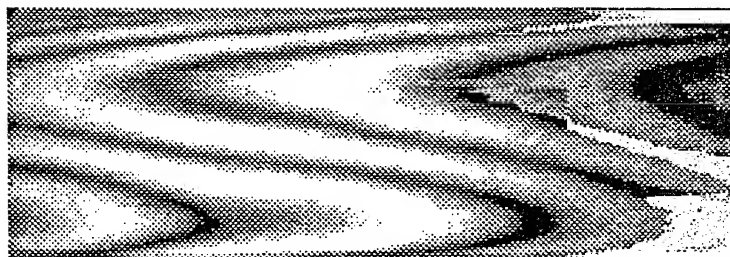
90° Projection

Figure 4.5: Steady State Patterns for Ra=6000
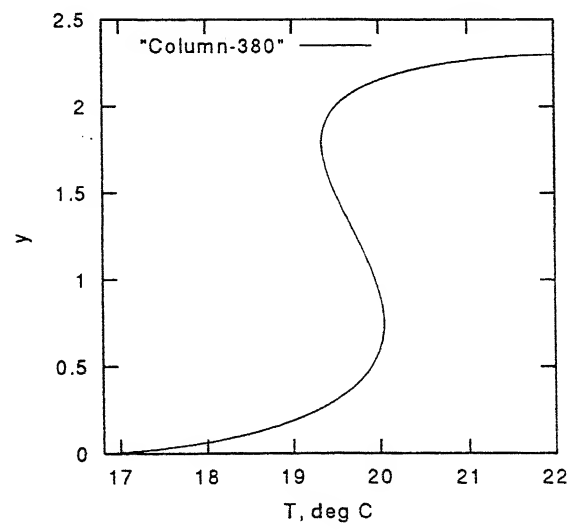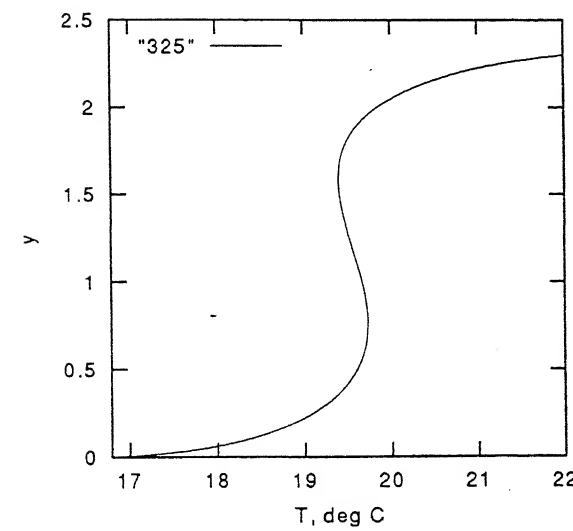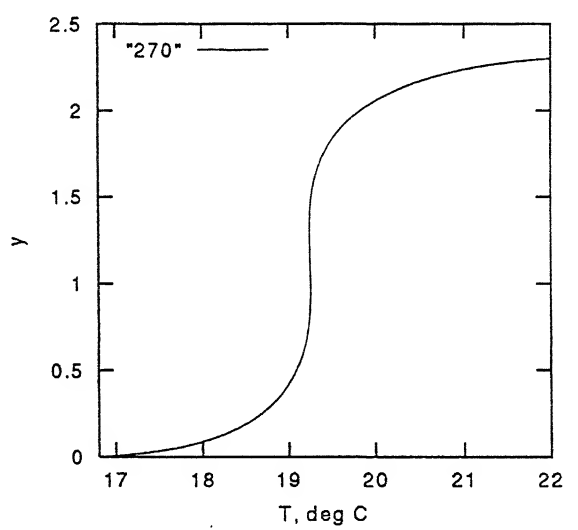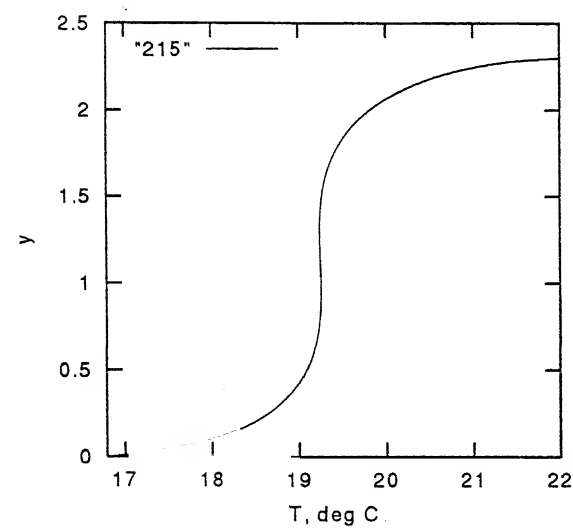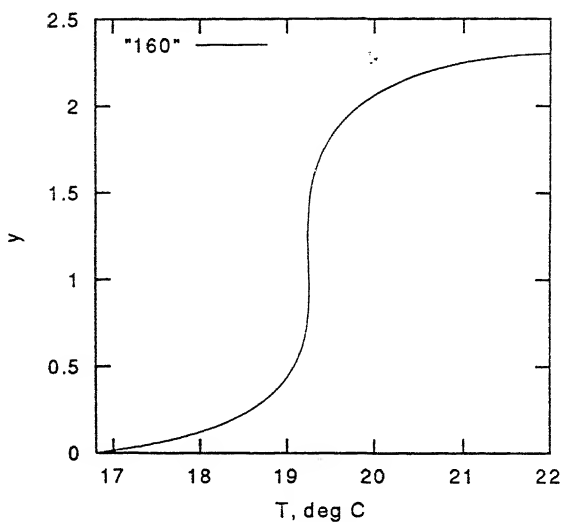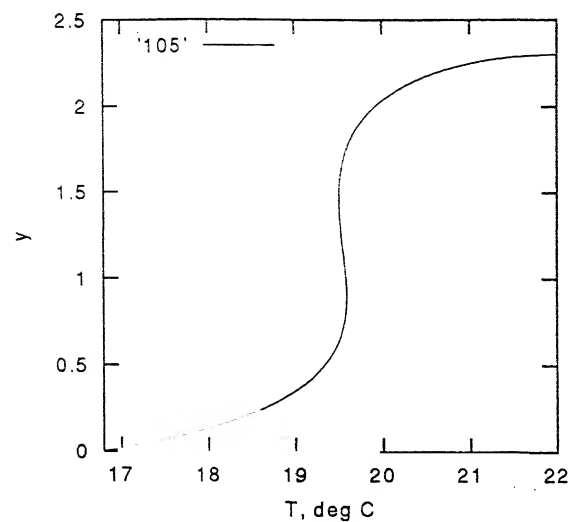
Figure 4.6: Temperature Variation as function of Vertical coordinates
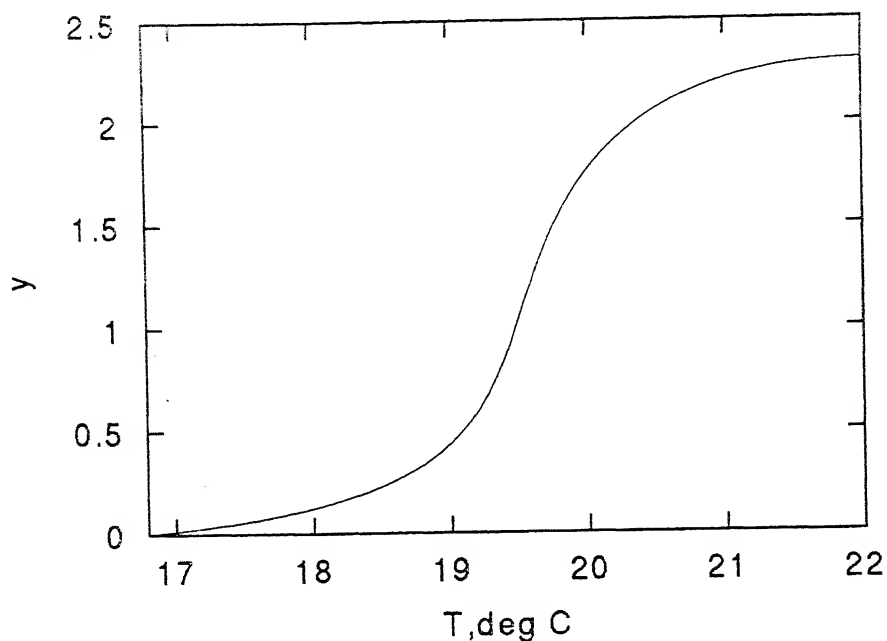
Figure 4.7: Width-Averaged Temperature Profile from the Interferogram, Ra=6000

4.2   Convection at Ra=8000

Analysis of the flow field observed with Ra=8000 is presented in this section. At this Rayleigh number there was a definite increase in the number of fringes as compared to those with Ra=6000. Here the fringe patterns of the square cavity observed by Mishra *et al.* (1998) were clearly visible during the early stages of the experiment. Mild unsteadiness was observed after 12 hours in the flow field. Thus it was a dynamic steady state with slight sideways movement of the fringes, a phenomenon which was absent for Ra=6000.

4.2.1   Transient Evolution of the Flow field

The pattern evolution process for Ra=8000 is shown in Figure 4.8. As seen from the interferograms, the flow field initially contains nearly straight fringes which are parallel to the walls of the cavity except in the central region. Figure 4.8(b) shows the fringe patterns similar to those observed with the experiments in square cavity. It shows the formation of two complete rolls in the central region of the cavity. The flow field is in a transient state and the fringes tend to deform to S-shaped curves with the passage of time as observed in Figures 4.8(c), 4.8(d) and 4.8(e). There is an increase in the number of fringes as the flow field reaches the steady state. Over a substantially longer period of time of about 11 hours, the flow field reaches a dynamic steady state where mild unsteadiness was observed. The fringes exhibited slight sideways movement. But there was no change in the overall pattern of the fringe field with respect to time. These dynamic steady state images are shown in Figures 4.8(g) and 4.8(h). The flow field is almost similar to that observed with Ra=6000 except the differences in the number of fringes and the mild unsteadiness of the flow field.
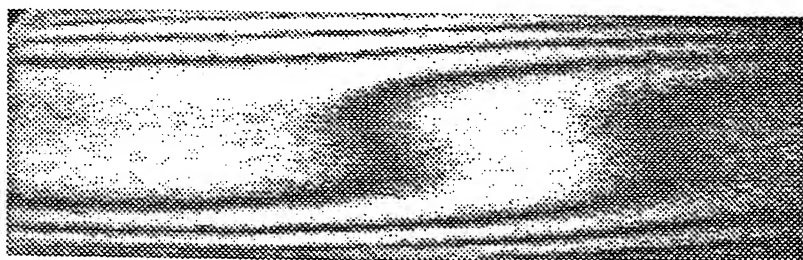
Fig.4.8(a)   1hour 30min
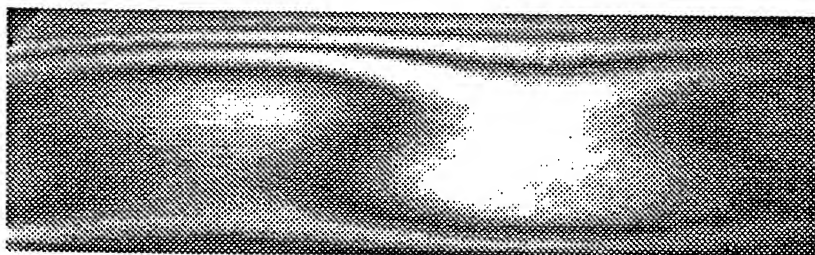
Fig.4.8(b)   3hours
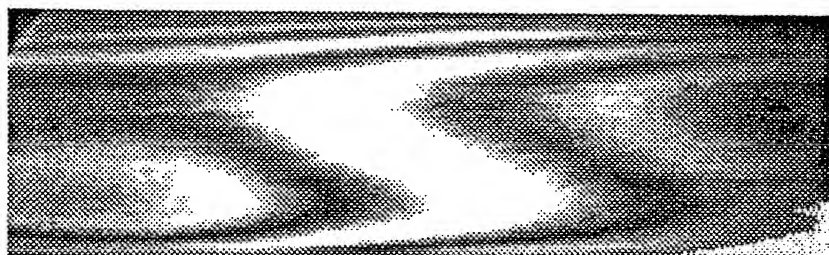
Fig.4.8(c)   4hours 20min

For Caption see next page
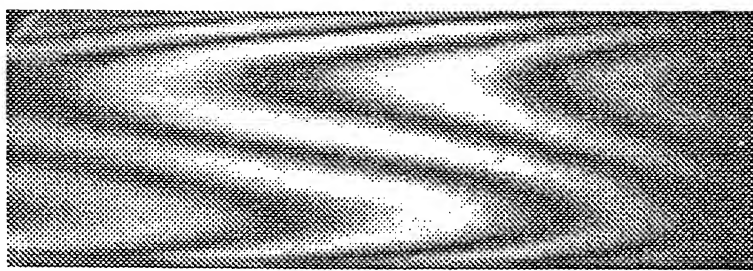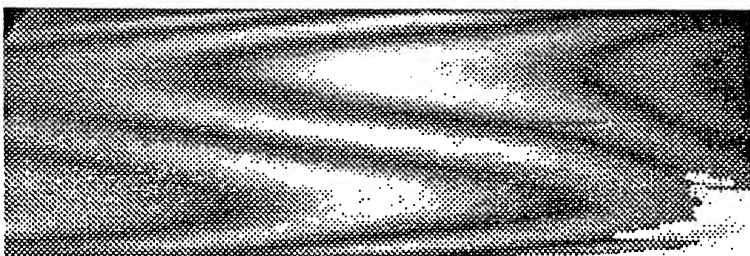
Fig.4.8(g)   11hours

Fig.4.8(h)   11hours 30min

Figure 4.8: Pattern Evolution for Ra=8000

Fig.4.8(d)   5hours

Fig.4.8(e)   6hours 30min
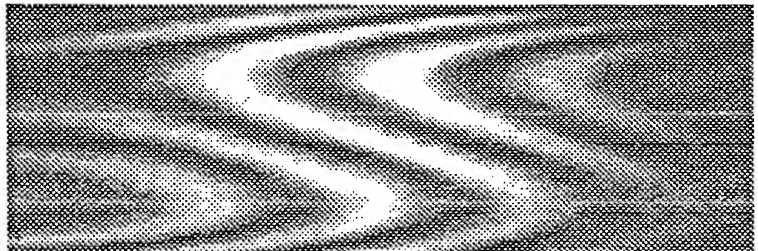
Fig.4.8(f)   8hours 20min

For Caption see next page

4.2.2   Axisymmetry of the Flow field

Interferograms collected from three diferent angles of $0°$, $45°$ and $90°$ are shown in Figure 4.9. The flow field exhibits a definite pattern and is quite similar in all the three projections shown. Fringe spacings and the number of fringes are very similar in all the three interferograms except in one of the three projections shown. This difference may be attributed to the fact that the flow field was in the dynamic steady state and slight movement of the fringes was present at the time of recording the interferograms. Due to this reason, one or two fringes might have got lost at the time of recording of the interferograms. Overall, an identical number of fringes were observed from all the three view angles at the time of experiments.

Variation of temperature field with respect to the vertical distance of the cavity have been plotted for equally spaced columns of the interferograms and are shown in Figure 4.10. Figure 4.11 shows the width-averaged temperature profile over a horizontal plane as a function of the vertical coordinate. As seen, the slopes of the S-shaped curves at the top and bottom walls are practically equal which reflects the fact that the net heat transfer across the cavity is a constant. This represents energy balance at the steady state.

0°

45°
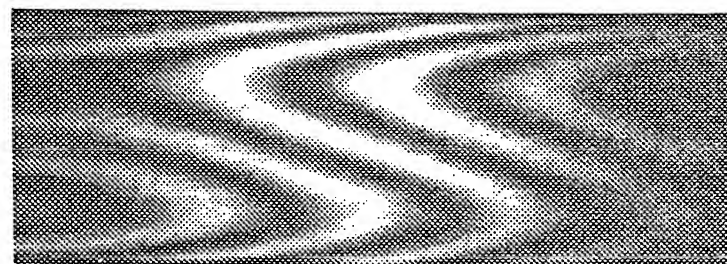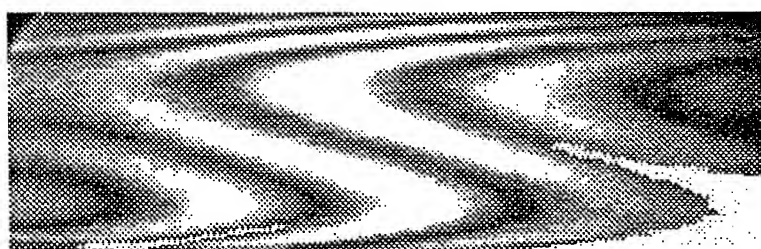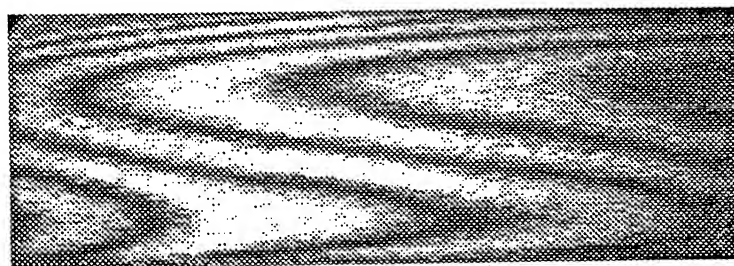
90° Projection

Figure 4.9: Steay State Patterns for Ra=8000
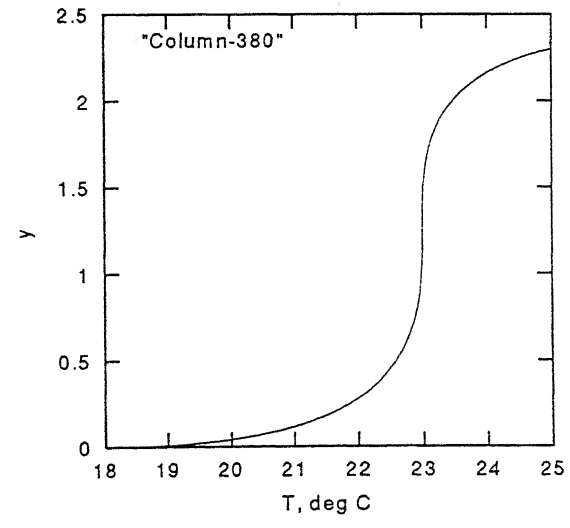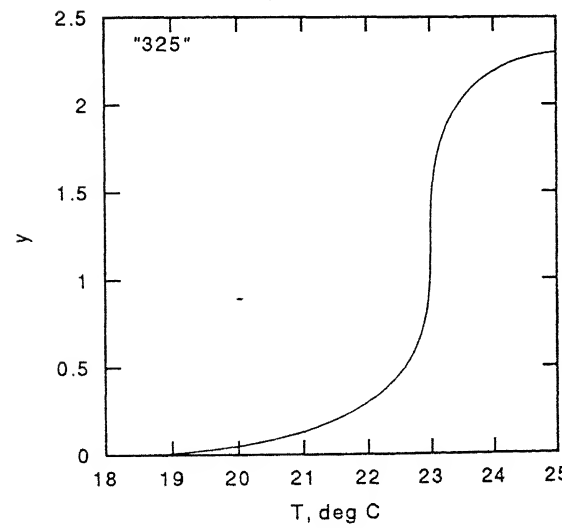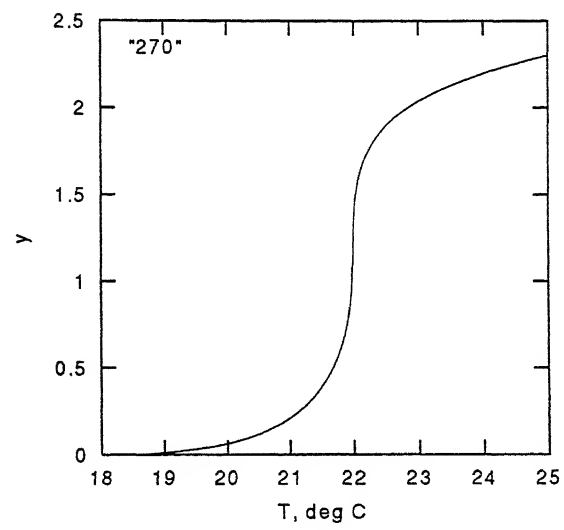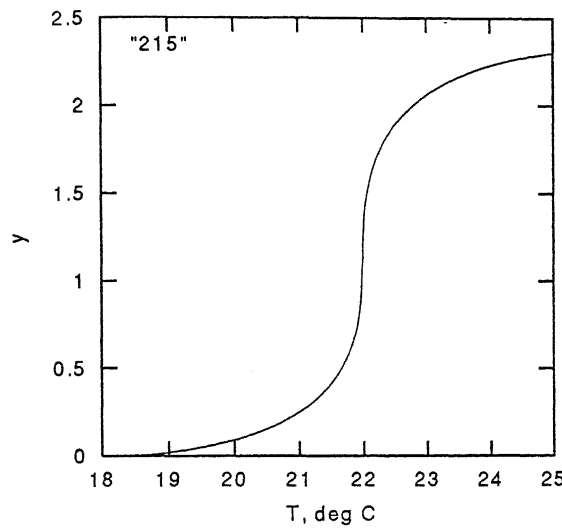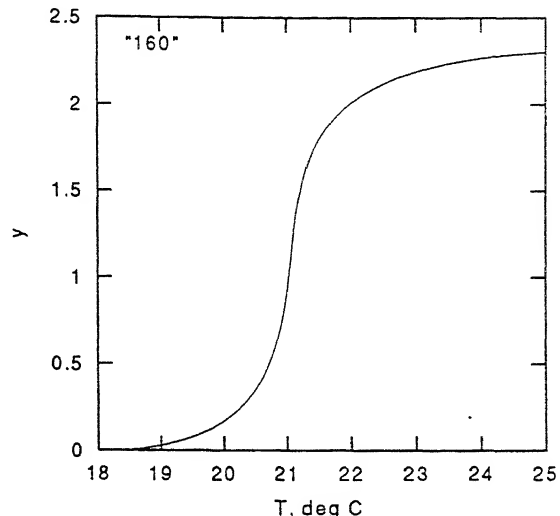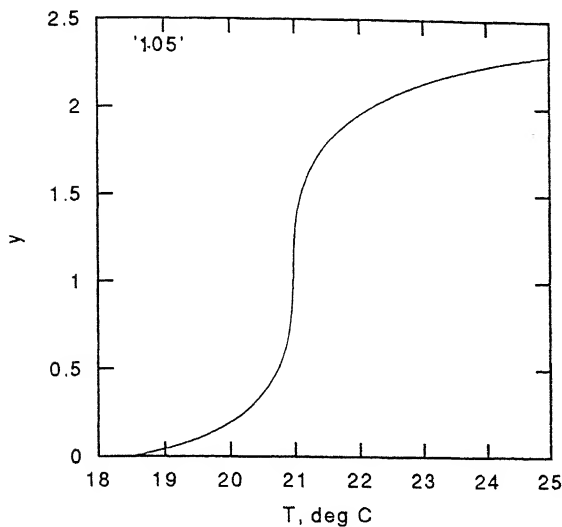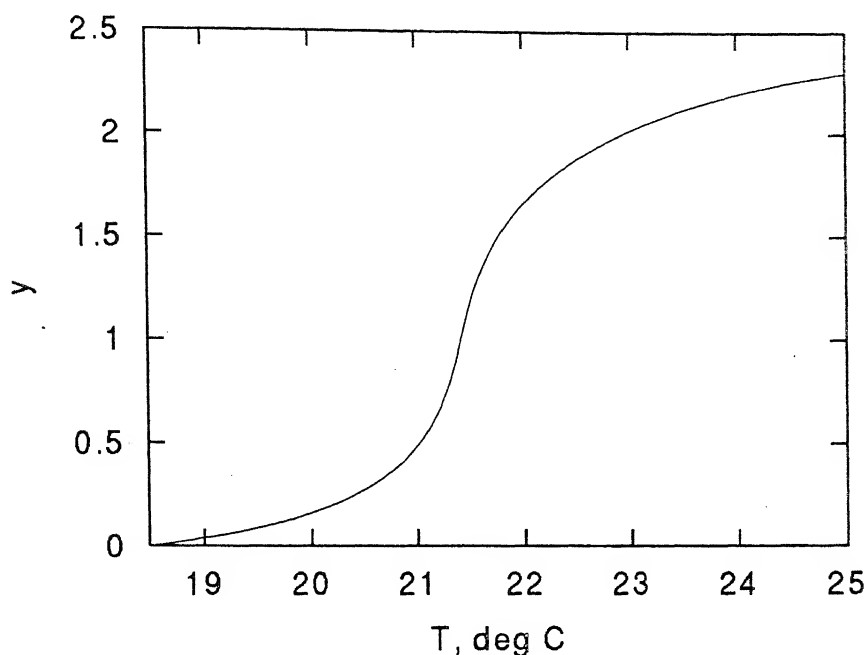
Figure 4.11: Width-Averaged Temperature Profile from the Interferogram, Ra=8000

4.3   Convection at Ra=10,000

Analysis of the flow field at Ra=10,000 is presented in this section. The experiments with this value of Rayleigh number were run for a longer duration of about 12 hours. During the transient evolution of the flow pattern, roll formation was observed at one moment and on the other moment these rolls were observed to straighten up in the form of straight fringes. The final flow field was found to be in dynamic steady state with the sideways movement of the fringes more pronounced as compared to that with lower values of Rayleigh numbers.

4.3.1   Transient Evolution of the Flow Field

Figure 4.12 shows the route of evolution of the flow pattern for Ra=10,000. The interferograms (Figure 4.12(b) and Figure 4.12(c)) show the formation of complete rolls at the top and bottom walls of the cavity. These rolls were seen to straighten up to give straight fringes during the transient state of the flow field as seen in Figures 4.12(d), 4.12(e) and 4.12(f), a phenomenon which was not observed in the experiments with Ra=6000 and Ra=8000. The flow field comprises of straight fringes before going into dynamic steady state where some time dependence was observed and the fluid layer showed mild unsteadiness. Interferograms collected after a substantially longer duration are shown in Figures 4.12(g) and 4.12(h). There is a definite increase in the number of fringes as the flow field evolves with time. It consisted of nearly 7-8 fringes once the dynamic state is reached. At this state the lateral movement of the fringes was clearly seen though the overall nature of the fluid layer was a constant with respect to time.
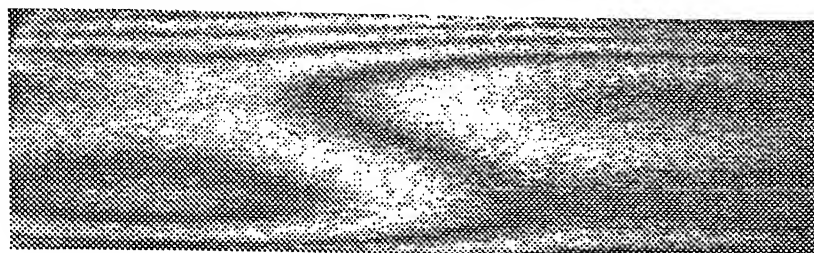
Fig.4.12(a) 1hour

Fig.4.12(b) 3hours

Fig.4.12(c) 4hours 30min

For Caption see next page
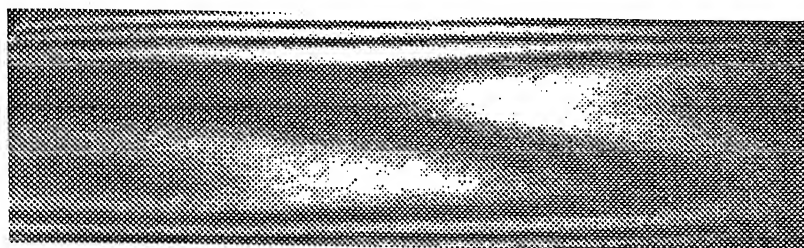
Fig.4.12(d)   5hours
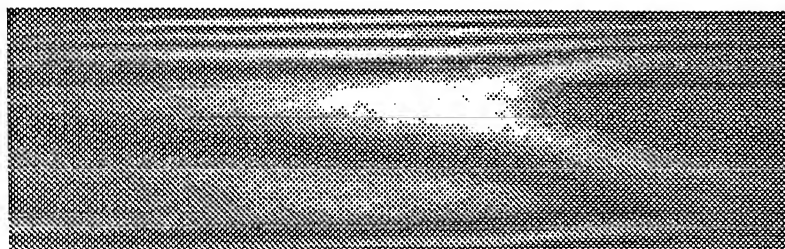
Fig.4.12(e)   6hours 30min


Fig.4.12(f)   8hours 40min

For Caption see next page
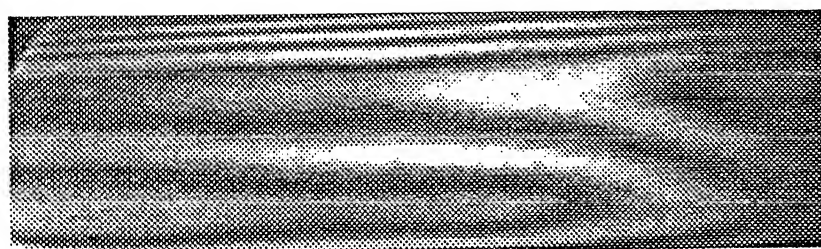
Fig.4.12(g)   11hours 30min

Fig.4.12(h)   12hours

Figure 4.12: Pattern Evolution for Ra=10,000

4.3.2 Axisymmetry of Flow Field

Figure 4.13 shows the interferograms collected from three different view angles in order to check the axisymmetric nature of the fluid layer. As seen the fringes exhibit a definite pattern in all the three projection data. The flow field was in dynamic steady state and due to the sideways movement of the fringes, which was quite dominant at Ra=10,000, the fringe spacings may not seem to be exactly equal in all the three interferograms but the overall behaviour and pattern of the fluid field was similar at steady state. In quantitative terms, however axisymmetry may be taken to have broken down at Ra=10,000.

Figure 4.14 shows the temperature variation plot as a function of the vertical coordinate of the cavity at six different equally spaced columns along the length of the test region. The y coordinate is measured from the cold top wall. The temperature measurements at each of these six columns were averaged over a horizontal plane and were plotted as a function of the vertical coordinate. This width-avaraged temperature profile is shown in Figure 4.15. The S-shaped curve is the characterestic of buoyancy- driven convection in differentially heated fluid layers.

0°

45°
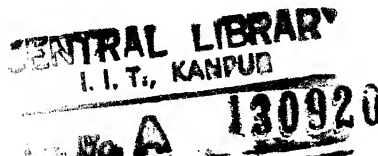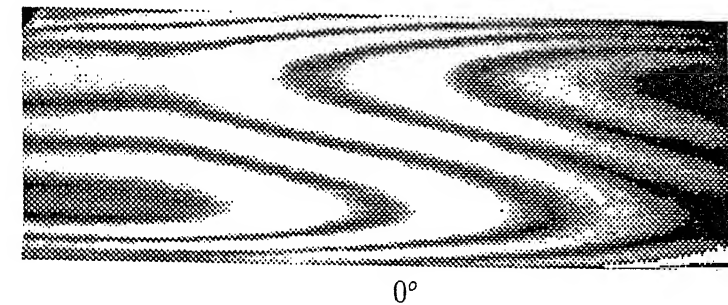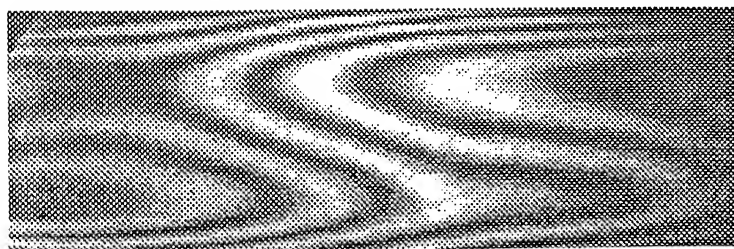
90° Projection

Figure 4.13: Steady State Patterns for Ra=10,000
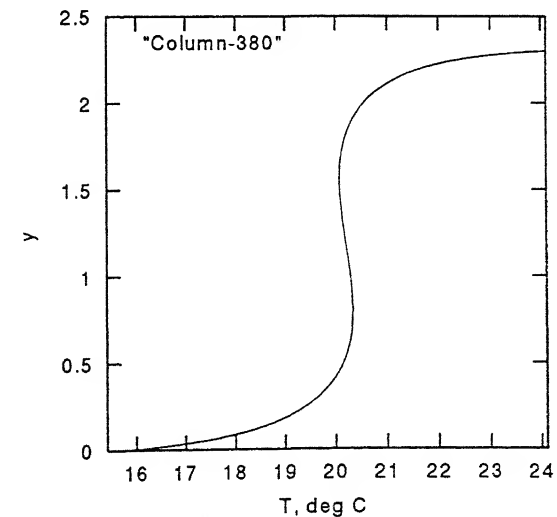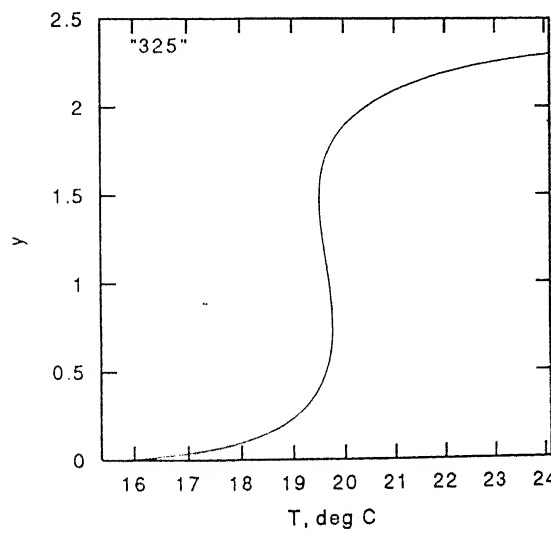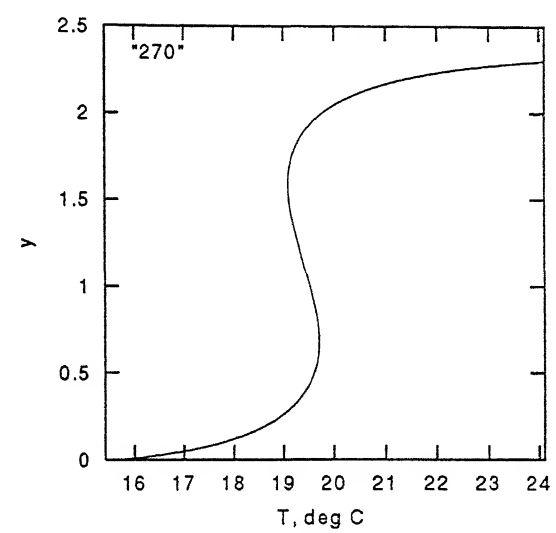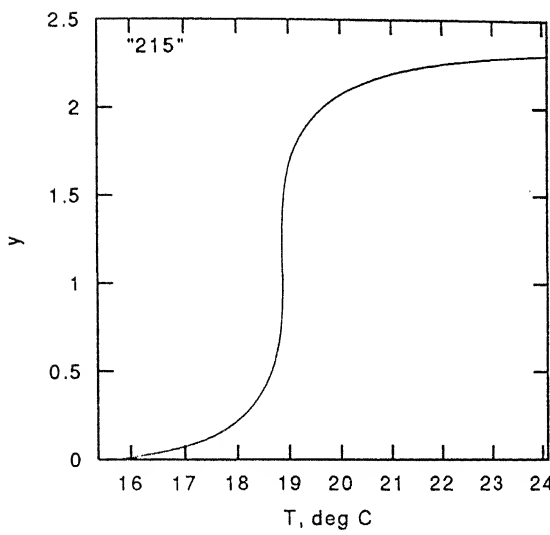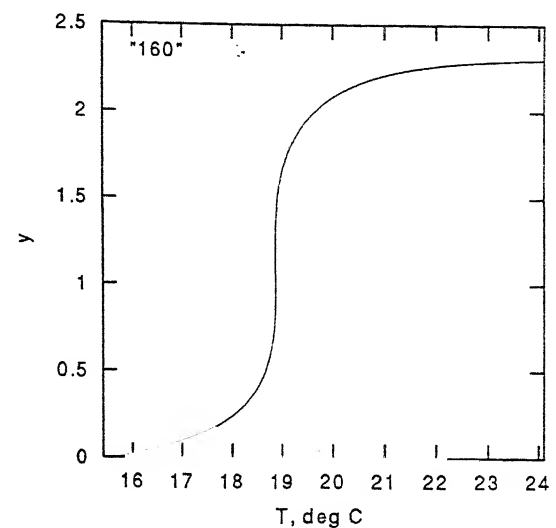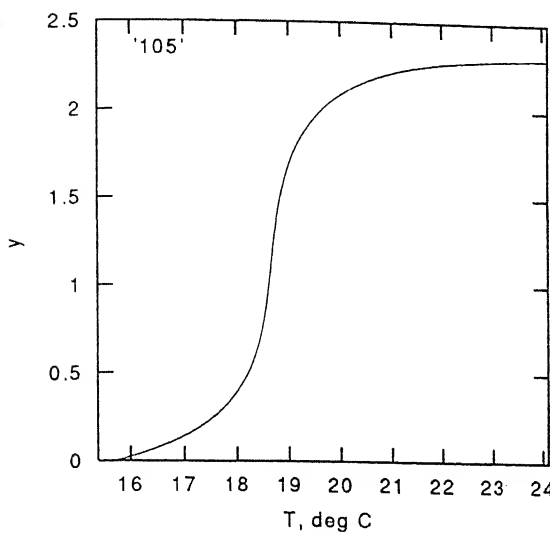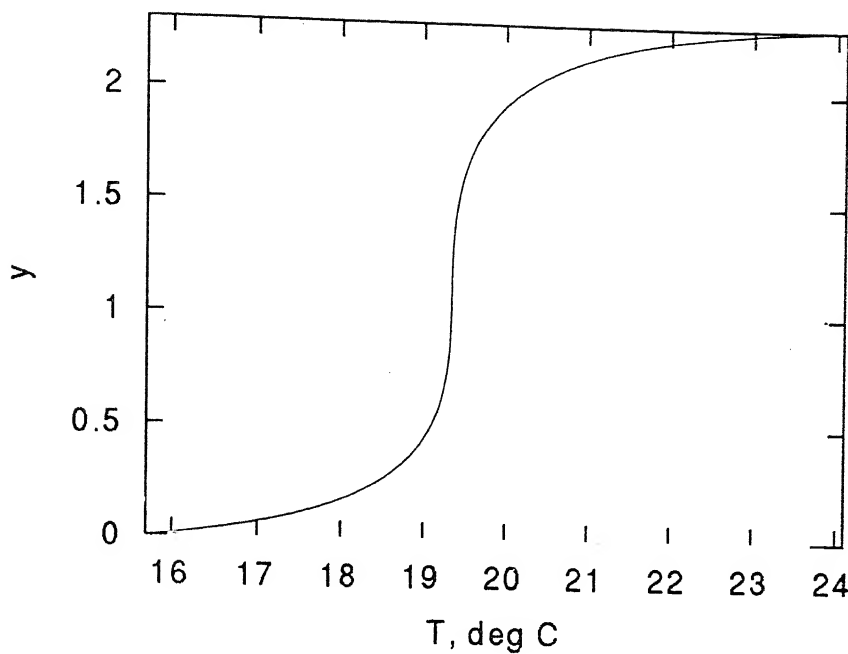
Figure 4.15: Width-Averaged Temperature Profile from the Interferogram, Ra=10.000

4.4 Convection at Ra=12,000

In this section, convection phenomenon at Ra=12,000 is discussed. The discussion includes both qualitative as well as quantitative analysis of the flow field. Heat transfer rates in terms of the average Nusselt number at the top and bottom walls of the cavity, temperature variation as a function of the vertical coordinate for $0°$ and $45°$ projections have been reported.

4.4.1 Transient Evolution of the Flow Field

At Ra=12,000 the fringes exhibited some time dependence. During the transient evolution the flow was seen to switch between two modes of convection of which one was more dominant than the other, a phenomenon which was not seen in the experiments with lower values of Rayleigh numbers. There was only a momentary appearance of the other mode and due to the limitations in the instrumentation it was not possible to capture it. All the interferograms that have been shown represent the dominant mode of the flow field.

Figure 4.16 shows the pattern evolution phenomenon of the flow field at Ra=12,000. As seen the flow consists of nearly straight fringes during the early stages of the experiments (Figure 4.16(a)). As the field evolves, these straight fringes deform to give roll-like structures which can be seen from Figure 4.16(b) and Figure 4.16(c). The number of fringes also increase as the fluid reaches the dynamic steady state. Figures 4.16(g) and 4.16(h) represent the flow field at dynamic steady state. Mild unsteadiness was observed after a substantially longer duration of about 12 hours and the fringes exhibited sideways movement. This was more prominent than that observed with Ra=10,000. The overall pattern of the fluid layer was almost similar to that seen with lower values of Rayleigh numbers except the number of fringes (about 9-10 at Ra=12,000) are much more due to the higher value of the temperature difference between the two plates. In order to ensure a record at steady state, three to four interferograms were collected after about 12 hours of the experimental time and all those revealed the same pattern as shown in Figure 4.16(h).
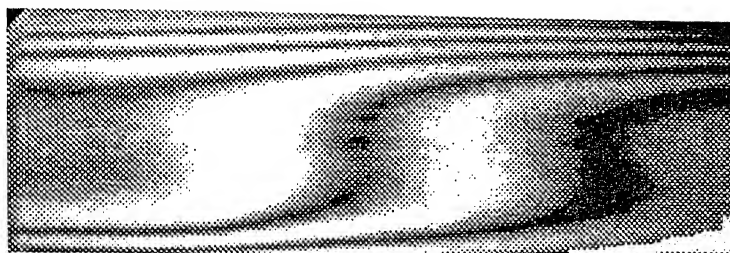
Fig.4.16(a)   1hour 25min
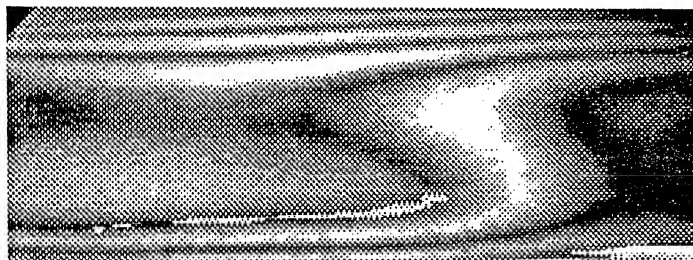

Fig.4.16(b)   3hours

Fig.4.16(c)   4hours 30min

For Caption see next page
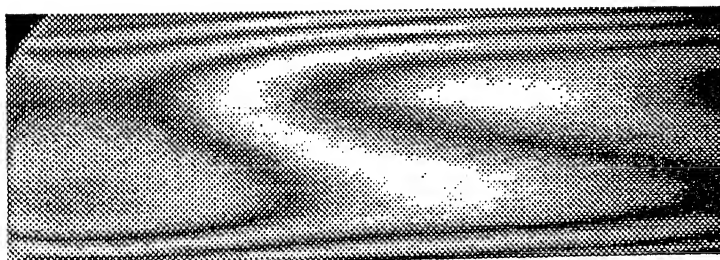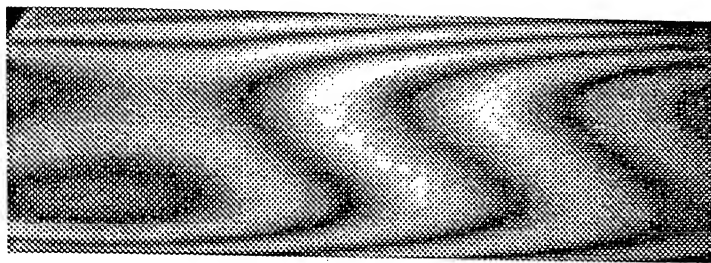
Fig.4.16(d)   6hours

Fig.4.16(e)   8hours 30min


Fig.4.16(f)   9hours

For Caption see next page
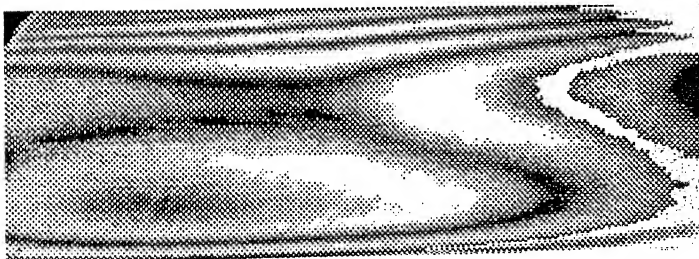
Fig.4.16(g)   10hours 40min


Fig.4.16(h)   12hours

Figure 4.16: Pattern Evolution for Ra=12,000
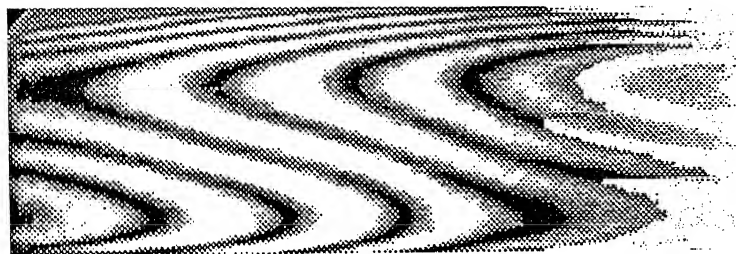
4.4.2   Axisymmetry of the Flow Field

Figure 4.17 shows the interferograms in the form of projections taken from $0°$, $45°$ and $90°$ angles. All the images show the steady state nature of the flow field. Due to the mild unsteadiness present and sideways movement of the fringes, the fringe spacings may not appear to be the exactly same from all the three projection angles but the overall pattern and the number of fringes are the same in all the interferograms. This establishes the axisymmetric behaviour of the flow field in qualitative (but not quantitative) terms.

Figure 4.18 and Figure 4.19 show the temperature variation as a function of the vertical distance of the cavity at six equally spaced columns along the length of the fluid layer for $0°$ and $45°$ projection angles respectively. These temperature values were averaged over a horizontal plane and the width-averaged temperature profile was plotted as a function of the vertical distance for both the projection angles. This width-averaged temperature profile is shown in Figure 4.20. Both the plots show similar trends, and have equal slopes at the walls.

0°

45°
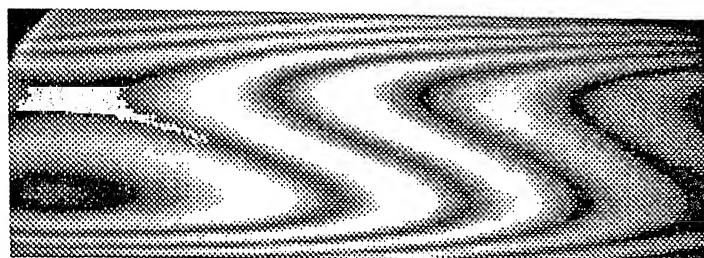
90° Projection

Figure 4.17: Steady State Patterns for Ra=12,000

the vertical coordinate y measured from the cold wall

'105'

"160"

"215"

"270"

"325"

"Column-380"

of Vertical coordinate measured from the cold wall
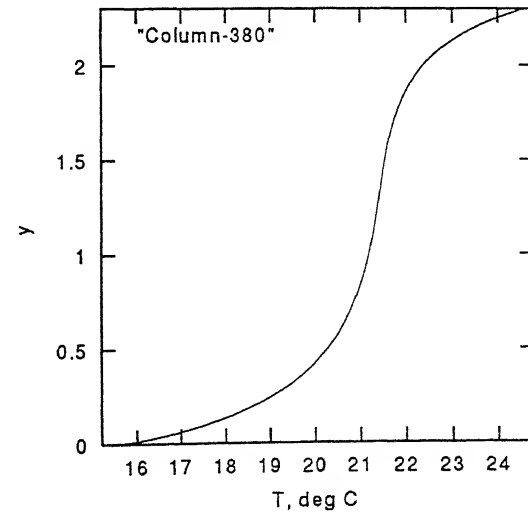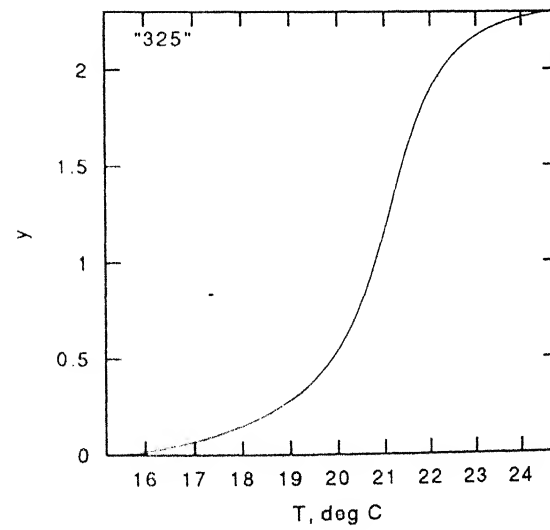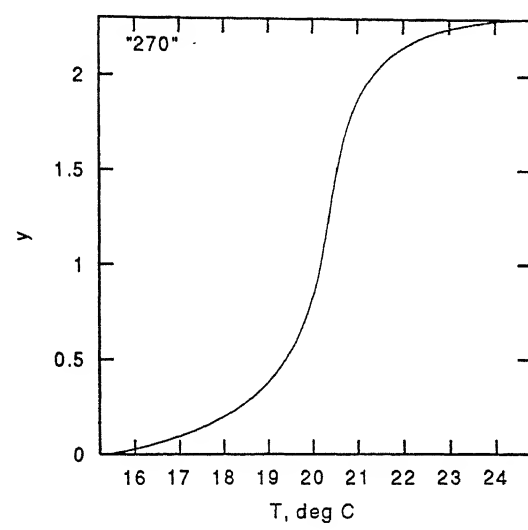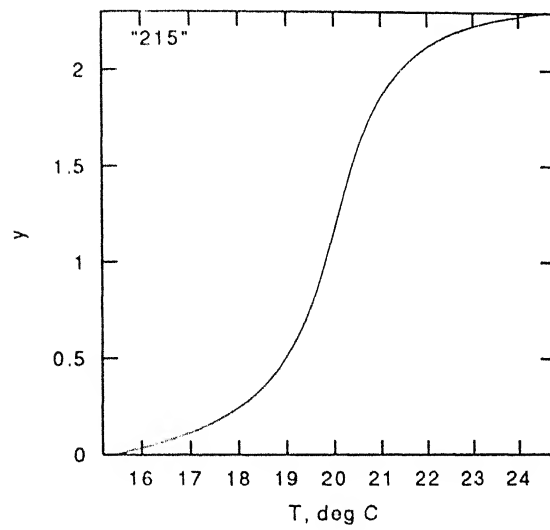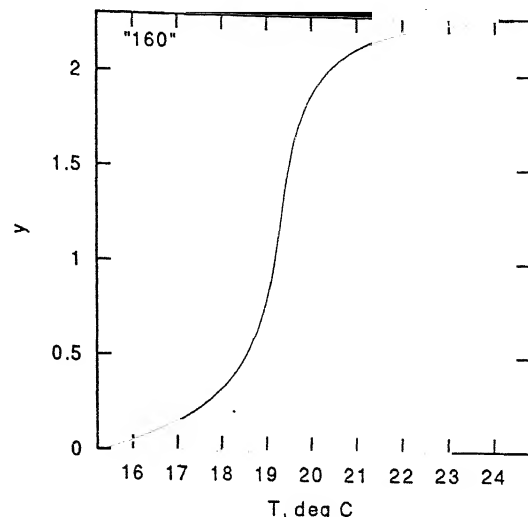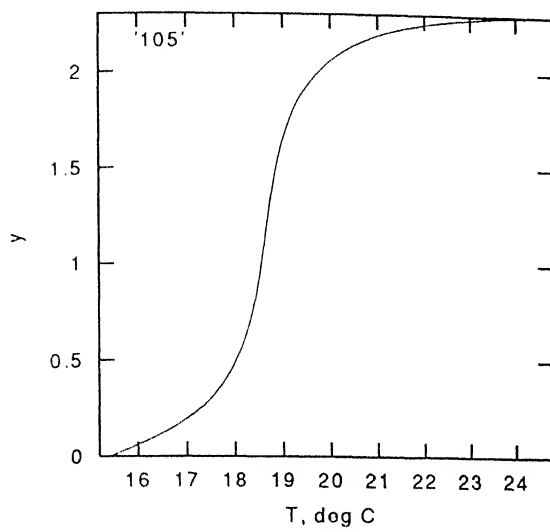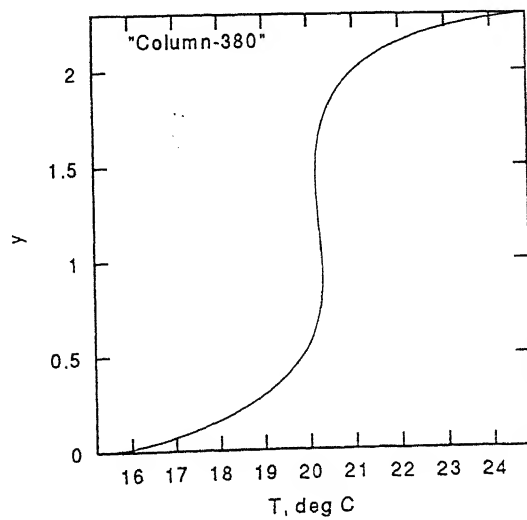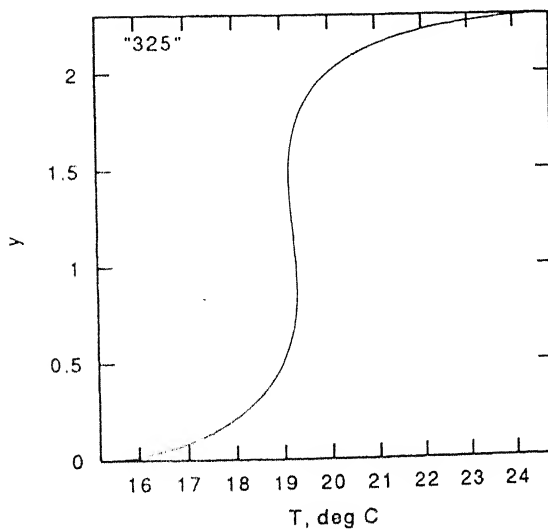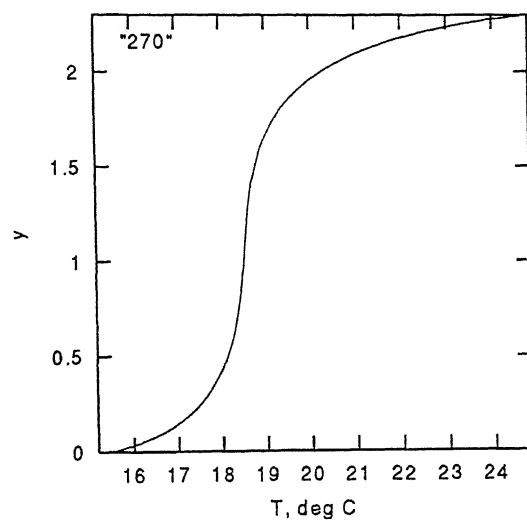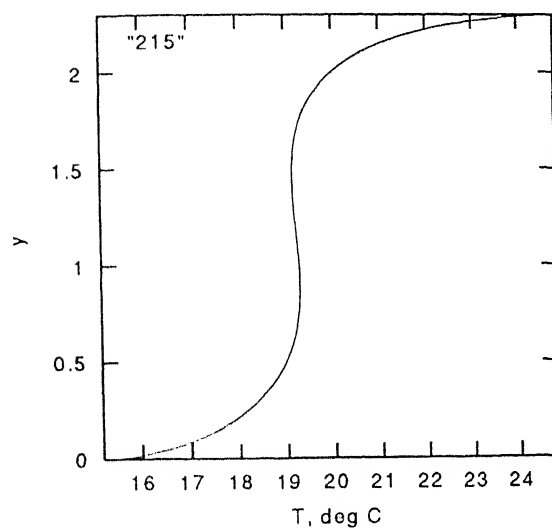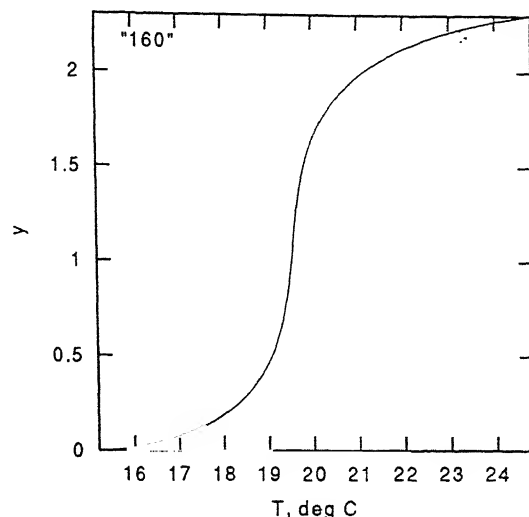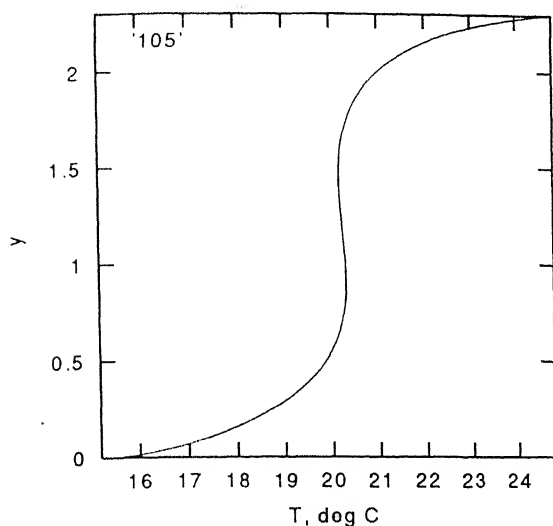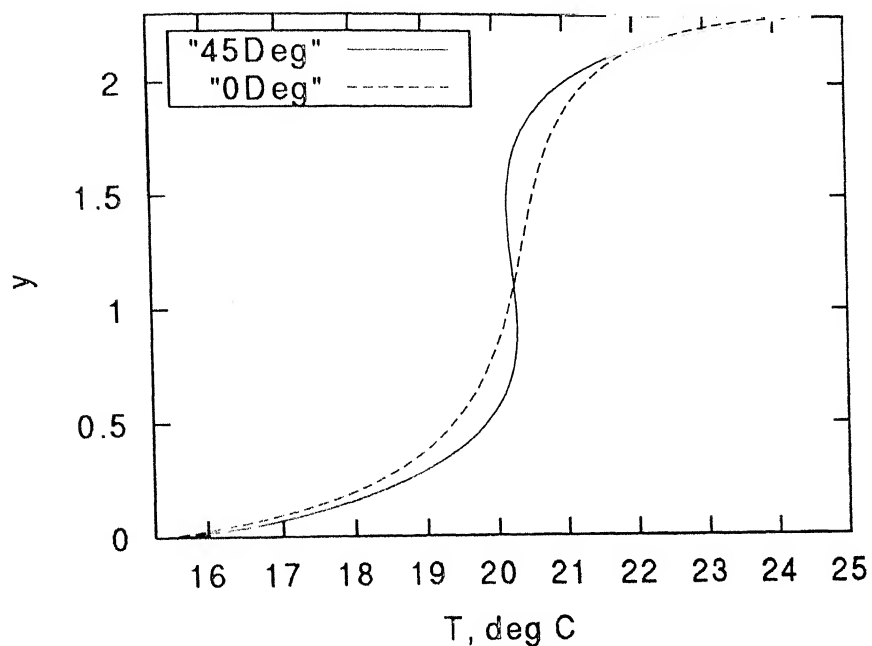
Figure 4.20: Width-averaged Temperature Profile from the Interferogram, Ra=12,000

4.4.3　Average Heat Transfer Rate

For Ra=12,000, heat transfer rates at the boundary walls have been reported in terms of average Nusselt number defined as

$$
Nu = \frac{-h}{T_{hot} - T_{cold}} \frac{\partial T}{\partial y} \Big|_{y=0,h}
\tag{4.1}
$$

The average Nusselt number for one projection angle (0°) is calculated.

Figure 4.21 shows the variation of average Nusselt number at the top and bottom walls of the cavity.
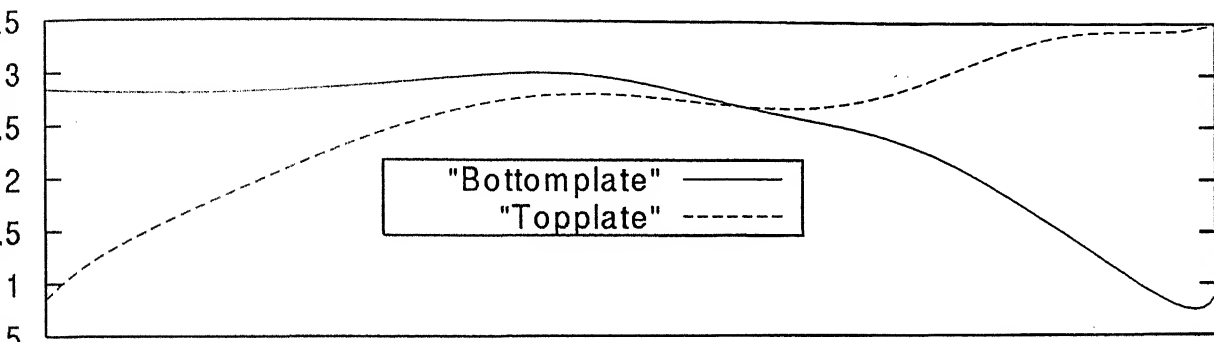
Figure 4.21: Nusselt Number Variation at the Top and Bottom Walls of the cavity, Ra=12,000

The individual plate-averaged Nusselt numbers for Ra=12,000 are 2.48 and 2.38 at the cold and the hot surfaces respectively of the cavity. The average Nusselt number for each of the plates has also been compared with the experimental correlation given by Gebhart *et al.* (1988), Chapter 3, Equation 3.14. The value of average Nusselt number as calculated from Equation 3.14 is 2.51 (with ±20% uncertainty) at Ra=12,000. Hence the Nusselt number calculated in the present experiment matches well with the reference correlation.

4.5 Discussion

Interferograms collected over a Rayleigh number range of 6000-12,000 reveal the following trends:

Upto Rayleigh number of 10,000, the fringe patterns after the elapse of sufficiently long amount of time are steady. Beyond Rayleigh number of 10,000 the fringes show definite movement indicating the attainment of dynamic steady state. Structurally the isotherm patterns are similar at all the Rayleigh numbers studied, differences appearing only in the form of a time dependence (not counting the increase in the number of fringes with the increased temperature difference). Similarly, axisymmetry is pronounced for Rayleigh numbers less then 10,000, as seen from the interferograms at various angles. Axisymmetry is lost in a quantitative sense (though not qualitatively) for Rayleigh numbers greater than and including 10,000. In all the experiments the width averaged steady state temperature profile showed good energy balance for heat transfer from the lower to the upper plate. The local temperature profiles in the fluid layer were seen to be physically meaningful.

The descent of the cold fluid from the top plate and its ascent from the lower heated surface requires that a roll pattern be setup in the fluid layer (Figure 4.22). Correlated with this roll pattern is a thermal field where the isotherms rise with the hot fluid and descent with the cold. In the interferograms presented in the previous sections, the upwelling of flow is to the extreme right while the fluid descent is to the exterme left. Two additional interferograms highlighting these effects at a Rayleigh number of 10,000 are shown in Figure 4.22 . The roll patterns symbolising the streamlines have also been shown.
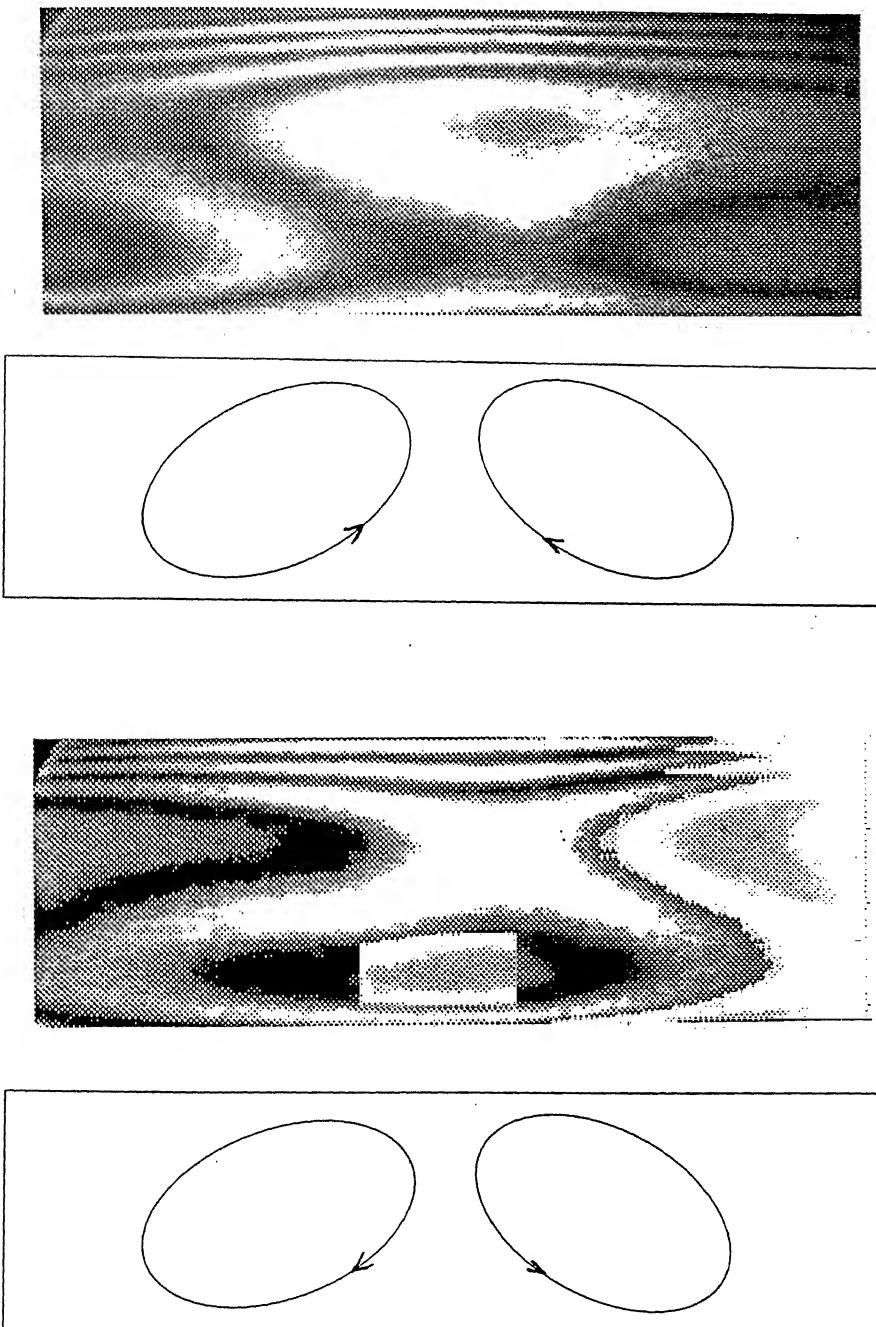
Figure 4.22: Isotherms and Roll Patterns at Ra=10,000

Chapter 5

Conclusions and Scope for Future Work

5.1 Conclusions

Rayleigh Benard convection in a differentially heated axisymmetric fluid layer has been experimentally studied using a Mach-Zehnder interferometer. Four different Rayleigh numbers equal to 6000, 8000, 10,000 and 12,000 have been considered. In order to establish the axisymmetric nature of fluid layer, three values of projection angles equal to $0°$, $45°$ and $90°$ have been used. The following conclusions have been drawn in the present work:

1. Steady fringe patterns were observed in the fluid layer in the Rayleigh number range 6000-12,000 after the passage of 10-12 hours.

2. The shape of the isotherms was preserved, going from one Rayleigh number to the next. The fringe spacing however decreased with increase in Rayleigh number and hence resulting in an increase in the number of fringes.

3. The fringe patterns remained invariant with respect to the projection angle. Thus the thermal field displayed axisymmetry in a broad sense, except for the variation within a roll.

4. The transient evolution of the thermal field took place over a substantially longer time scale compared to a square cavity of Mishra *et al.* (1998). In

fact, fringe patterns of the square cavity were seen to be reproduced in the axisymmetric fluid layer for short times during the early stages of the experiments. This observation supports the idea that the delayed transition has its origin in the distant proximity of the insulating side walls.

5. The isotherms reveal roll patterns in the fluid layer, with the formation of plumes at the roll-roll interface.

6. A good agreement between the experiments and numerical simulation has been achieved.

5.2   Scope for Future Work

There are quite a few important issues that can be addressed in the future as far as basic problem of Rayleigh-Benard convection is concerned. These are:

1. The three-dimensional temperature field can be reconstructed for the axisymmetric flows by using the tomographic algorithms.

2. The experiments at much higher Rayleigh numbers can be performed in order to visualise the fully unsteady convective field in axisymmetric geometries and can be compared with the results available for the square geometries.

3. The problem of Rayleigh-Benard convection can be studied for the two-phase flow.

4. Velocity field can be computed from the temperature data available in the form of projections.

Bibliography

[1] Bhadra S.K., Biswas G., and Muralidhar K., Reconstruction of the Temperature Field in Rayleigh-Benard Convection in a Cylindrical Cavity Using Interferometry, Proceedings of the Third ISHMT-ASME Heat and Mass Transfer Conference, IIT Kanpur, pp 747-752, 1997.

[2] de Bruyn J.R., Bodenschatz E., Morris S.W., Trainoff S.P., Hu Y., Cannel D.S., and Ahlers G., Apparatus for the Study of Rayleigh- Benard Convection in Gases Under Pressure, Rev. sci. Instrumentation, Vol. 67(6), pp 2043 2067, 1996.

[3] Forbes S.J., Numerical Inversion of Axisymmetric Interferograms, Experimental Heat Transfer, Vol. 9, pp 49-60, 1996.

[4] Gebhart B., Jaluria Y., Mahajan R.L. and Sammakia B., Buoyancy-induced Flows and Trasport, Hemisphere Publishing Corporation, New York, 1988.

[5] Gollub J.P. and Benson S.V., Many Routes to Turbulent Convection, Journal of Fluid Mechanics, Vol. 100, Part 3, pp 449-470, 1980.

[6] Krishnamurti R., On Transitions to Turbulent Covection, Part 1, The Transitions from two to three dimensional Flow, Journal of Fluid Mechanics, Vol. 42, Part 2, pp 295-307, 1970a.

[7] Krishnamurti R., On the Transitions to Turbulent Convection, Part 2, The Transitions to Time-Dependent flow, Journal of Fluid Mechanics, Vol. 42, Part 2, pp 309-320, 1970b.

[8] Michael Y.C. and Yang K.T., Three-dimensional Mach-Zehnder Interferometric Tomography of the Rayleigh-Benard Problem, ASME Journal of Heat Transfer, Vol. 114, pp 622-629, 1992.

[9] Mishra D., Muralidhar K., and Munshi P., Performance Evaluation of Fringe Thinning Algorithms for Interferometric Tomography, Optics and Lasers in Engineering, Vol. 30, pp 229-249, 1998.

[10] Mishra D., Muralidhar K., and Munshi P., Interferometric Study of Rayleigh-Benard Convection using Tomography with Limited Projection Data, to appear in Experimental Heat Transfer, Vol 12(2), pp 117-136, 1999.

[11] D. Mishra, K. Muralidhar and P. Munshi, Isotherms in a Horizontal Differentially Heated Cavity at Intermediate Rayleigh Numbers, International Communications in Heat and Mass Transfer, Vol. 26(5), pp 729-738 1999.

[12] Mishra D., Muralidhar K., and Munshi P., A Robust MART Algorithm for Tomographic Applications, Numerical Heat Transfer **B** (Fundamentals) Vol. 35 (4), pp 485-506 1999.

[13] Mishra D., Muralidhar K., and Munshi P., Interferometric Study of Rayleigh-Benard Convection at Intermediate Rayleigh Numbers, Fluid Dynamics Research, Vol. 25(5), pp 231-255, 1999.

[14] Mishra D., Muralidhar K., Munshi P., Laser Interferometry for Measurement of Three Dimensional Temperature Fields in Fluids using Tomography, Defence Science Journal, Vol. 49, pp 243-355, 1999.

[15] Mukutmoni D. and Yang K.T., Flow Transitions and Pattern Selection of the Rayleigh-Benard Problem in Rectangular Enclosures, Sadhna, Vol. 19, Part 5, pp 649-670, 1994.

[16] Mukutmoni D. and Yang K.T., Thermal Convection in Small Enclosures: An Atypical Bifurcation Sequences, Int. Journal of Heat and Mass Transfer, Vol. 38, Part 1,pp113-126, 1995a.

[17] Mukutmoni D. and Yang K.T., Pattern Selection for Rayleigh-Benard Convection in Intermediate-aspect-ratio Boxes, Numerical Heat Transfer, Part A, Vol. 27, pp 621-637, 1995b.

[18] Muralidhar K., Patil V.B. and Kashyap R., Interferometric Study of Transient Convection in a Square Cavity, J. of Flow Visualisation and Image Processing, Vol. 2, No. 4, pp 321-333, 1996.

Appendix A

Numerical Simulation of Rayleigh-Benard Convection Problem in Axisymmetric Geometries

The present appendix is concerned with the numerical solution of the buoyancy-driven flow in an axisymmetric geometry. The Rayleigh number chosen is Ra=6000. The dimensions of the test cell are the same as considered in the experimental work. Fluid considered is air with Pr=0.71. Due to the axisymmetric nature of the fluid cavity, the governing equations have been solved in $r - z$ coordinates system.

A.1 Governing Equations

The natural convection in any configuration is governed by the laws of conservation of mass, momentum and energy. These are mathematically represented by the continuity equation, Navier-Stokes equation and the energy equation, which in general form are as follows:

Continuity:

$$\frac{\partial u}{\partial r} + \frac{u}{r} + \frac{\partial v}{\partial z} = 0 \tag{A.1}$$

r-Momentum:

$$\rho\left[\frac{\partial u}{\partial t} + u\frac{\partial u}{\partial r} + v\frac{\partial u}{\partial z}\right] = -\frac{\partial p}{\partial r} + \mu\left(\frac{\partial^2 u}{\partial r^2} + \frac{1}{r}\frac{\partial u}{\partial r} - \frac{u}{r^2} + \frac{\partial^2 u}{\partial z^2}\right) \tag{A.2}$$

z-Momentum:

$$\rho[\frac{\partial v}{\partial t} + u\frac{\partial v}{\partial r} + v\frac{\partial v}{\partial z}] = -\frac{\partial p}{\partial z} + \mu(\frac{\partial^2 v}{\partial r^2} + \frac{1}{r}\frac{\partial v}{\partial r} + \frac{\partial^2 v}{\partial z^2}) + \rho_o g\beta(T - T_o) \quad (A.3)$$

Energy:

$$\rho c_p[\frac{\partial T}{\partial t} + u\frac{\partial T}{\partial r} + v\frac{\partial T}{\partial z}] = k(\frac{\partial^2 T}{\partial r^2} + \frac{1}{r}\frac{\partial T}{\partial r} + \frac{\partial^2 T}{\partial z^2}) \quad (A.4)$$

A.2   Non-dimensionalization

Various non-dimensional parameters used in the numerical simulation have been given below:

Reference Temperature: The temperature has been non-dimensionalised as

$$T = \frac{T - T_c}{T_h - T_c} \quad (A.5)$$

Reference Length: Since the height of the cavity h, plays the major role in the flow as the temperature variations and thus density variations responsible for buoyancy force due to gravity exist in the vertical direction. Hence the height of the enclosure is considered as the reference length for non-dimensionalization.

Reference Velocity: The non-dimensionalized velocity is taken as

$$V = \frac{\nu}{h} \quad (A.6)$$

Reference Pressure:

$$P = \rho(\frac{\nu}{h})^2 \quad (A.7)$$

The non-dimensional parameter responsible for the buoyancy induced flows in the cavity namely the **Grashoff** number is defined as

$$Gr = Ra/Pr$$

where Ra is the Rayleigh number and is defined as

$$Ra = \frac{g\beta(T_h - T_c)h^3}{\nu\alpha} \quad (A.8)$$

and Pr is the Prandtl number defined as

$$Pr = \frac{\nu}{\alpha} \quad (A.9)$$

A.3 $\psi - \omega - T$ Formulation

The u and v velocities have been defined as

$$u = \frac{1}{r}\frac{\partial \psi}{\partial z} \cdot$$
(A.10)

$$v = \frac{1}{r}\frac{\partial \psi}{\partial r}$$
(A.11)

One can now derive the following:

Stream Function Equation:

$$\omega = -\frac{1}{r}\left(\frac{\partial^2 \psi}{\partial r^2} - \frac{1}{r}\frac{\partial \psi}{\partial r} + \frac{\partial^2 \psi}{\partial z^2}\right)$$
(A.12)

Vorticity Equation:

$$\frac{\partial \omega}{\partial t} + u\frac{\partial \omega}{\partial r} + v\frac{\partial \omega}{\partial z} - \frac{u}{r}\omega = \frac{\partial^2 \omega}{\partial r^2} + \frac{1}{r}\frac{\partial \omega}{\partial r} + \frac{\partial^2 \omega}{\partial z^2} - \frac{1}{r^2}\omega + \frac{Ra}{Pr}\frac{\partial T}{\partial r} \quad \text{(A.13)}$$

Energy Equation:

$$\frac{\partial T}{\partial t} + u\frac{\partial T}{\partial r} + v\frac{\partial T}{\partial z} = \frac{1}{Pr}\left(\frac{\partial^2 T}{\partial r^2} + \frac{1}{r}\frac{\partial T}{\partial r} + \frac{\partial^2 T}{\partial z^2}\right)$$
(A.14)

A.4 Boundary Conditions

For computation, the temperature, stream function and vorticity boundary conditions can be represented as

Top Wall:

$$T = T_c$$
(A.15)

$$\psi = 0$$
(A.16)

$$\omega = -\frac{1}{r}\frac{\partial^2 \psi}{\partial z^2}$$
(A.17)

Bottom Wall:

$$T = T_h$$
(A.18)

$$\psi = 0$$
(A.19)

$$\omega = -\frac{1}{r}\frac{\partial^2 \psi}{\partial z^2}$$
(A.20)

Side Walls:

$$\psi = 0 \tag{A.19}$$

$$\frac{\partial T}{\partial r} = 0 \tag{A.20}$$

$$\omega = 0 \tag{A.21}$$

A.5   Initial Conditions

The following initial conditions have been applied:

$$\psi = 0 \tag{A.22}$$

$$\omega = 0 \tag{A.23}$$

$$T = linear \tag{A.24}$$

A.6   Numerical Scheme and Solution Procedure

The governing equations have been discretised using an implicit finite difference scheme. A uniform grid of 41×41 per convection cell is used. The convective terms of the momentum equations are discretized using the 2nd order upwind scheme while central difference discretisation has been applied to the diffusive terms. The matrix inversion is by the Gauss-Siedel method.

A.7   Results

The results of numerical simulation for Ra=6000 have been presented in this section. Figure A.1 and Figure A.2 show the numerically generated velocity vectors and streamlines for one cell of the fluid layer. As seen, these plots indicate the formation of one complete roll. Isotherms in the form of projection data have been plotted and are shown in Figure A.3. Figure A.4 shows isotherms in two adjacent cells and clearly indicates the formation of a complete roll. Figure A.5 shows the temperature variation as a function of vertical coordinates at three different equally spaced columns

length of the cavity. The width- averaged temperature profile is shown in Figure A.6. The S-shaped nature of the plot reveals the buoyancy-driven convective flow. The variation of nusselt number at the bottom wall is shown in Figure A.7. The average value of Nusselt number at the bottom wall is 2.17. For the same value of Rayleigh number i.e. Ra=6000, the average Nusselt number calculated from the experimental correlation given by Gebhart *et al.* (Equation 3.14) comes out to be 2.09 (with ±20% uncertainty). Hence the calculated value of average Nusselt number through numerical simulation matches well with the value obtained through the standard correlation.
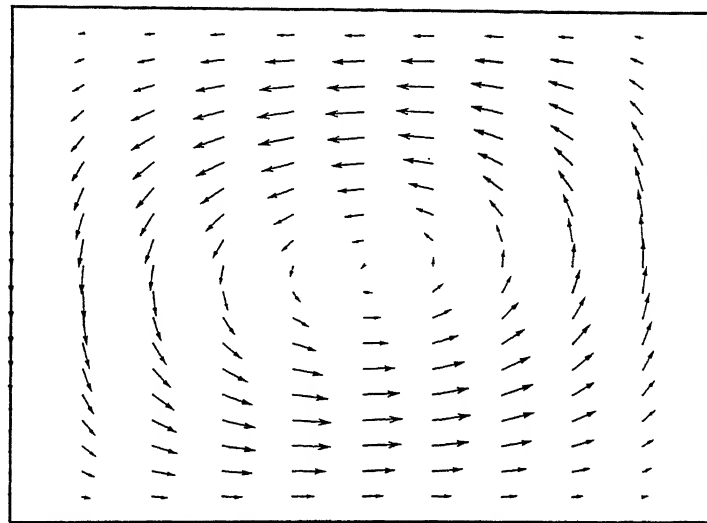
Figure A.1: Numerically Generated Velocity Vectors
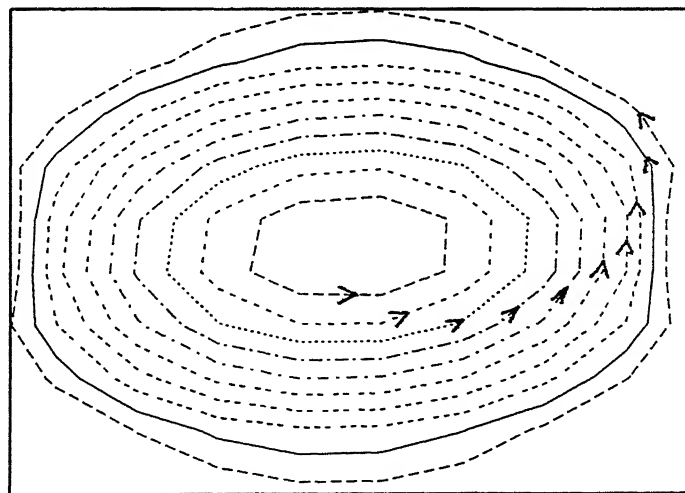
Figure A.2: Numerically Generated Streamlines, $\psi_{min} = 0$, $\psi_{max} = 91$
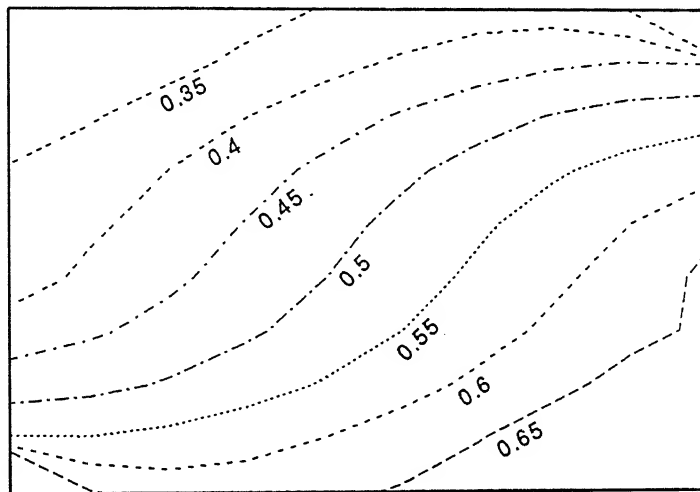
Figure A.3: Numerically Generated Isotherms, Ra=6000
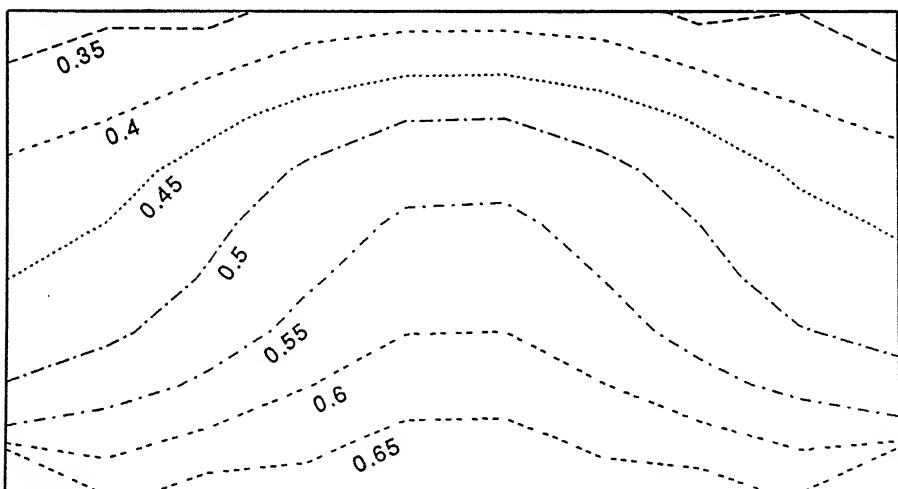
Figure A.4: Isotherms in two adjacent cells, Ra=6000
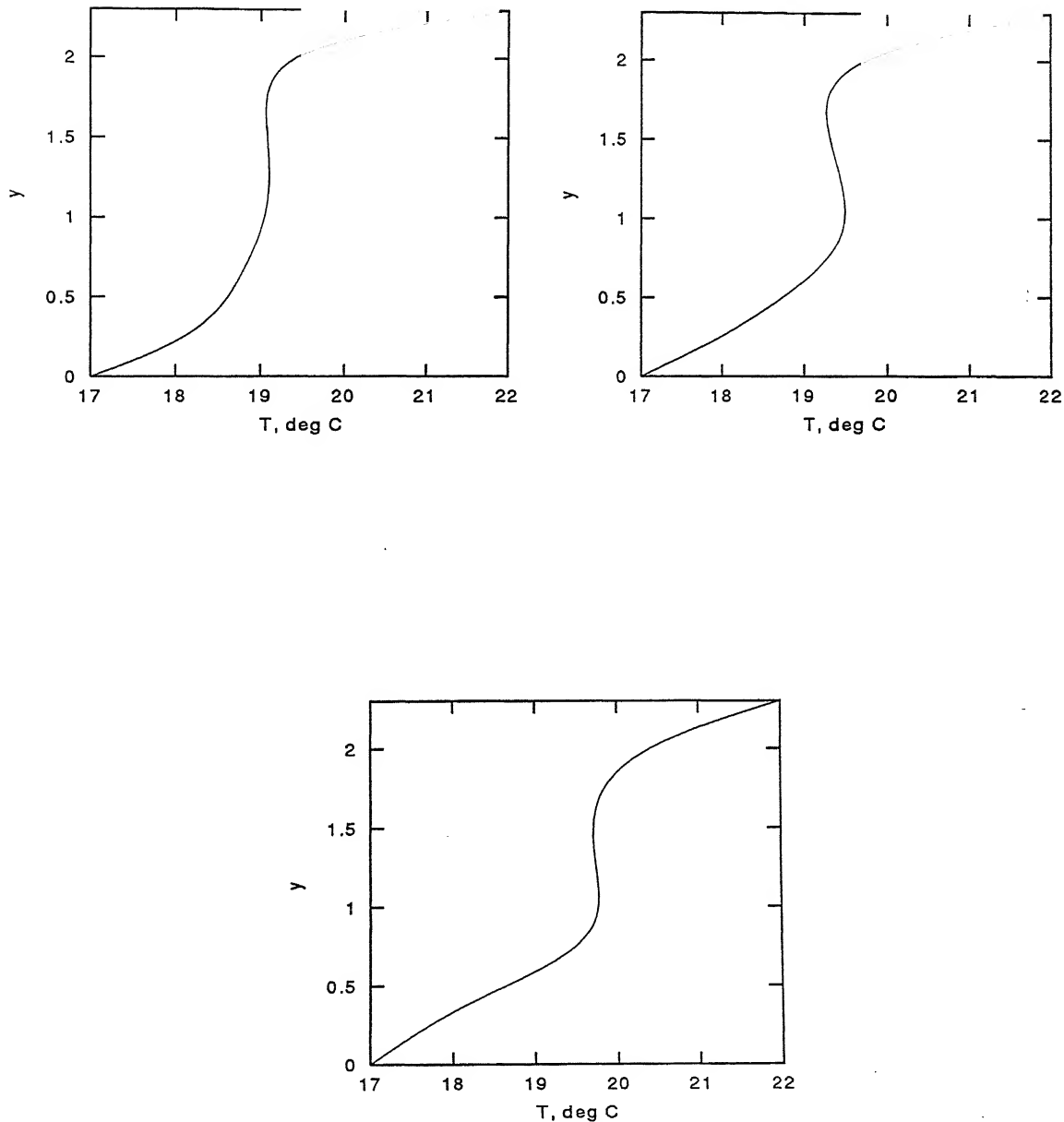
Figure A.5: Temperature Variation as a function of Vertical coordinates, Ra=6000
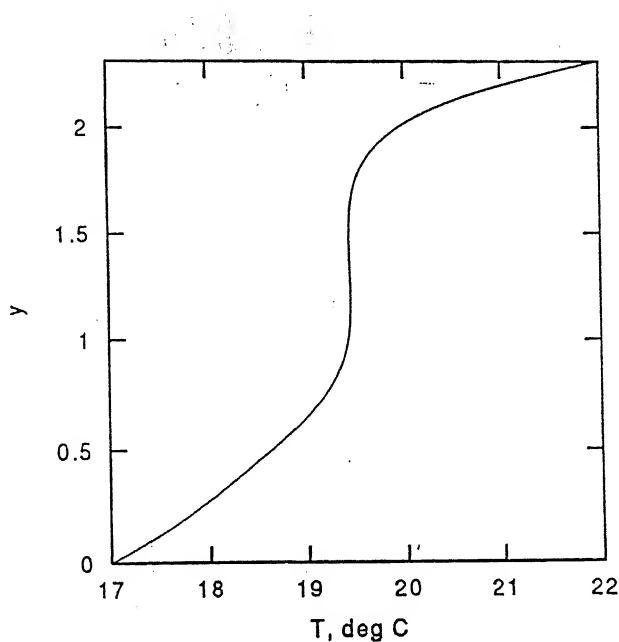
Figure A.6: Width-Averaged Temperature Profile, Ra=6000
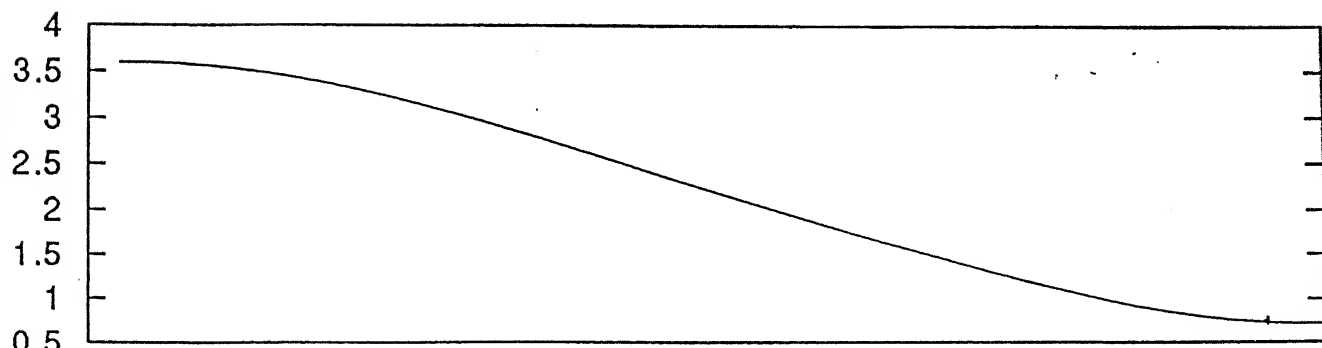
Figure A.7: Nusselt Number Variation at the Botom Wall, Ra=6000